A turbulent mixing layer constrained by a solid surface. Part 1. Measurements before reaching the surface

By D. H. WOOD† AND P. BRADSHAW

Department of Aeronautics, Imperial College, London

Extensive single- and two-point measurements have been made in a high-Reynolds-number single-stream mixing layer growing to encounter a wind-tunnel floor on its *high-velocity* side. The measurements include detailed conditionally sampled results, which separate the turbulent and irrotational contributions to the two-point covariances. These measurements show that the true (vorticity-bearing) large-scale structure in the isolated mixing layer, well away from the region influenced by the floor, is three-dimensional without a trace of the two-dimensional orderly structure found in some two-stream mixing-layer experiments. The structure appears to be a combination of the classical mixing jet and double-roller eddy (Grant 1958); the circulation in the latter is confined almost exclusively to the (x, z)-plane. The large spanwise scales in the potential motion are attributed to the effect of pressure disturbances and not to two-dimensionality of the turbulent structure, as claimed by previous workers. The first effect of the wall is to stretch the streamwise and spanwise scales of the large eddies. Near the high-velocity edge $\overline{u^2}$ is amplified more than $\overline{w^2}$. The surprising result that the low-wavenumber (large-eddy) contribution to $\overline{v^2}$ is amplified across the whole layer is associated with the nature of the mixing jets and the alteration of the pressure field by the wall. The change in turbulence structure occurs *before* any significant change in the mean-velocity profile, and the implications for the calculation of the change in boundary conditions are discussed. The measurements made after the mixing layer reached the wind tunnel floor will be presented in part 2.

1. Introduction

This paper is one of a series on 'complex' turbulent flows, defined as shear layers with complicating influences like distortion by extra rates of strain or interaction with another turbulence field. General reviews of complex flows are given by Bradshaw (1975, 1976). This paper is a companion study to that of Weir, Wood & Bradshaw (1981; hereinafter denoted by WWB) who measured the interacting turbulent mixing layers in a plane jet.

It is well known that the presence of a solid surface has a large effect on shear-layer structure. For computational purposes it is often necessary to distinguish between unbounded, 'free' shear layers, far away from a solid surface, and well-bounded flows, or 'wall layers' for short. For example, any representative lengthscale of the

---

† Present address: Department of Mechanical Engineering, University of Newcastle, N.S.W. 2308, Australia.

turbulence close to a solid wall must vary as the distance from the surface, but the scale is roughly constant across a free shear layer or across the outer part of a wall layer. Furthermore, the modelling of the unmeasurable pressure–strain term in the shear-stress transport equation must be altered significantly near a solid wall (e.g. Bradshaw 1973; Launder, Reece & Rodi 1975). Many important flows involve a change in species from a free shear layer to a wall layer and there have been many studies of flow over backward-facing steps (Chandrsuda & Bradshaw 1981 and references therein) and of impinging jets (e.g. Gutmark, Wolfstein & Wygnanski 1978 and references therein). However, it is difficult to separate the effects of the change in boundary conditions from the effects of recirculation and streamline curvature (Castro & Bradshaw 1976) in these experiments, and no detailed study has been made in a flow that remains a plane shear layer while it experiences the influence of a wall. The growth of a plane mixing layer to reach the wind-tunnel floor,† as shown in figure 1, is the simplest possible realization of such a flow, provided that the inevitable floor boundary layer remains negligibly thin. The mixing layer in this study was a single-stream layer in 'still air' (i.e. room air).

There is considerable controversy over the structure of a turbulent mixing layer; principally over the two-dimensionality or otherwise of the large eddies. Statements of the opposing views can be found in Roshko (1976) and Bradshaw (1980). The correlation measurements in §4 support the main conclusion of Chandrsuda *et al.* (1978), admittedly based on measurements in the same rig, that the quasi-two-dimensional large eddies, formed during transition, persist only in the absence of a mechanism to cause breakdown to three dimensionality.

It is to be expected that the effect of the wall on the large-eddy structure is to stretch the scales in the plane of the wall and to transfer turbulent energy from the normal component $\overline{v^2}$ into $\overline{u^2}$ and $\overline{w^2}$. The high- and low-Reynolds-number experiments of Thomas & Hancock (1978) and Uzkan & Reynolds (1967) respectively, on grid turbulence constrained by a solid wall moving at the free-stream velocity, showed that the influence of the 'no-slip' or 'viscous' constraint, that is $U = W = u = w = 0$ at the wall, was confined to a viscous region whose thickness is of the order of that of a laminar boundary layer. In the present experiment the viscous region is embedded in the thin floor boundary layer. Outside this region Thomas & Hancock found that $\overline{u^2}$ was amplified at the expense of $\overline{v^2}$. Obviously $V = v = 0$ at the wall by the 'image' or impermeability constraint, which, in contrast to the no-slip condition, affects the fluctuations out to a distance from the surface of the order of the wavelength of the large eddies. 'Inactive' motion in a turbulent boundary layer (Townsend 1961; Bradshaw 1967), which contributes to the u- and w-motion but not to the v-motion or to the shear stress, is caused by the same mechanism. Thomas & Hancock found that $\overline{w^2}$ was not significantly amplified, in disagreement with the rapid-distortion theory of Hunt & Graham (1978) for turbulence that is axisymmetric about the vertical axis, and the large-eddy simulation of Biringen & Reynolds (1981). Both these analyses predict equal amplification of $\overline{u^2}$ and $\overline{w^2}$, as does the simple theory of Wood & Ferziger (1982; hereinafter denoted by WF) for the potential flow in figure 1. Normal stresses presented in WF are in similar disagreement with the theory.

To the accuracy of neglecting the viscous constraint, which affects only the wall boundary layer, the present flow can be considered as the instantaneous interaction

---

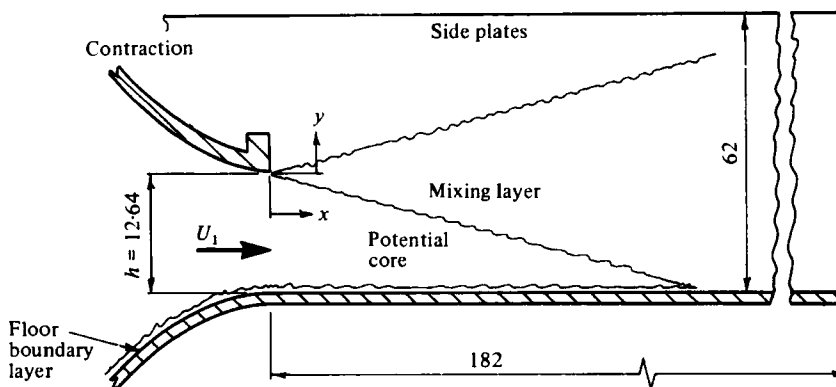† Convention forces us to equate 'floor', 'wall' and 'surface'.

FIGURE 1. Schematic diagram of test rig. All dimensions in cm.

of a turbulent mixing layer with its mirror image. The initial region of a plane jet was studied by WWB as the interaction of a mixing layer and its 'image' about the centreline, having the same mean, but not instantaneous, properties as the 'real' layer.

Section 2 briefly describes the experimental techniques and data reduction. The conditional-sampling routines, in particular the extension to two-point (correlation) measurements, are described in the appendix. Some of the single-point and two-point measurements taken from Wood (1980), where the experimental techniques are fully described, are presented in §§3 and 4 respectively. The experimental results are available on digital tape from either author; those taken after the mixing layer reached the floor are described in part 2.

2. Experimental techniques

All the measurements are made in a specially built working section fitted to a 76.2 cm $\times 12.7$ cm blower tunnel described by Bradshaw (1972). The free-stream velocity U_1 was 16.4 ± 0.1 m s^{-1} for all the measurements and the combination of free-stream turbulence and unsteadiness levels was 0.25% at small x. The working-section dimensions are shown in figure 1. Preliminary spanwise correlation measurements showed that the flow was not sensitive to a reduction to 30 cm in the height of the sidewalls, the insertion of a backplate above the contraction exit, or the installation of bellmouth fairings, like those shown in figure 1 of Wygnanski & Fiedler (1970), on the walls.

After considerable thought and experimentation, described in Wood (1980, chap. 3), we decided not to remove the floor boundary layer.

Total pressure was measured by a round Pitot tube of outside diameter $d = 1$ or 1.2 mm, and the static pressure was taken as atmospheric. The results were corrected by assuming that the effective centre was displaced by $0.15\,d$ in the direction of the mean shear. From the repeatability of the results in figure 2 the accuracy of the measurements is estimated at 1% of U_1. Standard hot-wire techniques were used. X-wire probes were calibrated statically in the potential core assuming a 'cosine-law' response to yaw, with the effective angle determined by calibration. Tests over a yaw range of $15°$ to $75°$ ($45 \pm 30°$ from the x-axis), reported in Wood (1980), showed this

procedure to be an excellent approximation. The hot-wire signals were simultaneously recorded on an Ampex FR 1300 analog tape recorder using an effective bandwidth of 1 Hz–10 kHz. The data were subsequently transcribed onto digital tapes for batch processing, including linearization, on the Imperial College computer, using the equipment and two-channel (single-point) program described by Weir & Bradshaw (1974). The large amount of computer time needed to analyse the data prevented the use of wholly satisfactory averaging times for the single-point measurements in §3. The time was, typically, 15 s of real time and was increased slightly with increasing x. Some of the scatter in the present results, especially in the u-component measurements, is attributable to the short averaging times used. The averaging time for the correlation measurements was typically 8 s, and the repeated points shown in the present results, usually at minimum separation, show that this was satisfactory. The accuracy of the total correlations is estimated as ± 0.05, unless stated otherwise.

   Two special programs were written to analyse the present data. The first computed the spectra (and then the autocorrelations as the inverse Fourier transforms of the spectra) from selected single-point data, and the second analysed the four-channel (two-point) data. Details of the first are not important here. However, we are not aware of any previous extension of single-point conditional sampling techniques to two-point measurements, so the details of the program are given in the appendix. More details of the experimental details and data-reduction techniques are given in Wood (1980). Notation is explained in the appendix.

3. Single-point results

3.1. *Initial conditions and mean-velocity profiles*

All the single-point measurements were taken along the midspan of the tunnel. The mean velocity in the initial boundary layer, measured just upstream of the lip, was reasonably close to the Blasius profile with a 99 % thickness of 2.4 mm. The momentum thickness θ_0 was 0.30 mm. The effective origin x_0 of the self-preserving mixing layer was found to be at $x = -6.8$ cm, that is, upstream of the lip as is the general case for initial laminar boundary layers. The mean-velocity profiles are shown in figure 2. Self preservation is achieved at roughly $x = 45$ cm, where $x/\theta_0 = 1500$ and $Re_x \equiv U_1 x/\nu = 4.8 \times 10^5$. This agrees with the criterion of $x/\theta_0 > 10^3$ of Bradshaw (1966), but not with his alternative suggestion that $Re_x > 7 \times 10^5$. The spreading rate is about 5 % less than that measured by Castro (1973) in the same wind tunnel at double the present U_1. Birch's (1980) survey recommends a value of $L = 0.115\,(x - x_0)$ for single stream mixing layers. L is the distance between the points where $U = \sqrt{0.9}\,U_1$ and $\sqrt{0.1}\,U_1$. The present value is $L = 0.103\,(x - x_0)$. The estimated thickness δ, defined as the distance between the points where $U = 0.995\,U_1$ and $0.005\,U$, is given by $\delta = 0.22\,(x - x_0)$. If anything, this low value of the spreading rate suggests that the present flow is subject to a minimum of external disturbances, such as flapping caused by intermittent alighting on the floor, which would *increase* δ and L. The presence of the wall does not alter the mean-velocity profile shape. Some spanwise non-uniformity in U was found. It appears to correlate with the spanwise non-uniformity of the initial boundary layer; it is a maximum around $x - x_0 = 36$ cm, and then decreases in magnitude roughly as $(x - x_0)^{-1}$. The reasons for this are explored in Wood (1982).
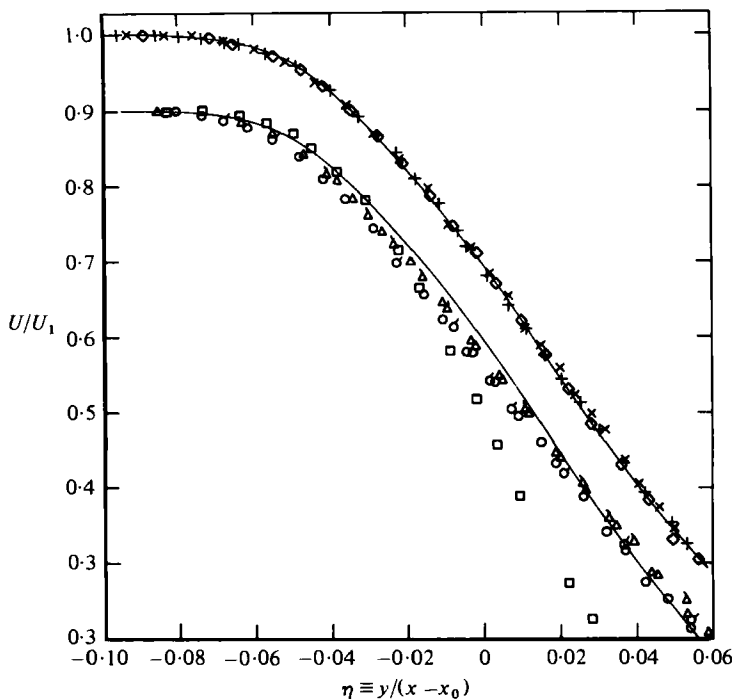
FIGURE 2. Mean-velocity profiles. □, $x - x_0$ (cm) = 13·56; ○, 26·49; △, 39·03; +, 51·83; ×, 64·59; ◇, 77·29. Flagged symbols are repeated measurements.

3.2. *Turbulence measurements*

The measurements of γ (see appendix) are shown in figure 3. The single-point values are generally slightly lower than those from the two-point measurements, probably because of the different hold times Δt, as explained in the appendix. γ also decreases slightly with increasing x. This behaviour is believed to be genuine because $\Delta t \omega_{\mathrm{K}}$ increases with x and so would increase the measured γ if the interface statistics remained unaltered.

The downstream development of the normal stresses is shown in figure 4, together with the distributions from Castro (1973), which Rodi's (1973) survey concluded are reliable data. The rise in $\overline{u^2}$ with x near the high-velocity edge for $x > 62$ is partially caused by the increasing level of potential fluctuations in the diminishing potential core. WF show that the potential flow is unaffected by the wall, over the measured range of η, for $x < 24$ cm. For example, at $\eta = -0.051$, $\overline{u^2}$ increases by a factor of 1·8 between 24 and 100 cm. Over this distance $(1-\gamma)\,\overline{u_{\mathrm{N}}^2}$, which contributes 20 % to $\overline{u^2}$ at 24 cm, increases by nearly 2·7 times, while $\gamma\overline{u_{\mathrm{T}}^2}$ increases by a factor of nearly 1·6.[†] Away from this region the results are self-preserving to within the accuracy of measurement. However $\overline{v^2}$ is self-preserving only for the first three stations. After 50 cm it increases across the *whole* layer, a result repeated in later checks in another test rig. This totally unexpected behaviour occurs when $\delta/h < 0.8$. The only previous

[†] Here $(1-\gamma)\,\overline{u_{\mathrm{N}}^2}$ and $\gamma\overline{u_{\mathrm{T}}^2}$ are the non-turbulent (N) and turbulent (T) contributions to $\overline{u^2}$ as defined by the addition law of equation (A 1) of the appendix.
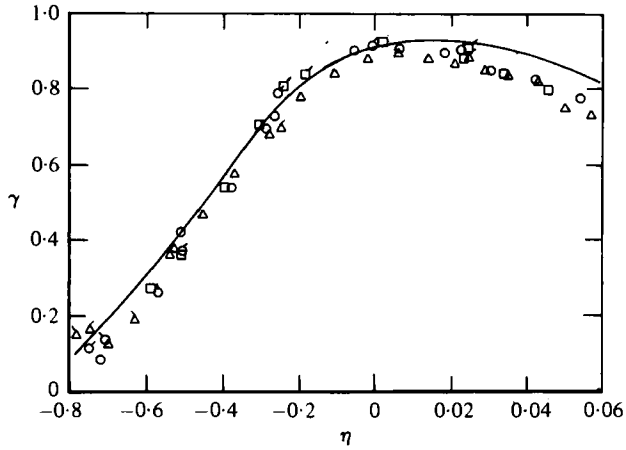
FIGURE 3. Intermittency factor. Nominal $\square$, $x-x_0$ (cm) $= 24$; $\bigcirc$, 36; $\triangle$, 75. Left and right facing flagged symbols from normal and spanwise correlations respectively. Unflagged symbols are single-point results. Solid line from Castro (1973), $x-x_0 = 56$ cm.
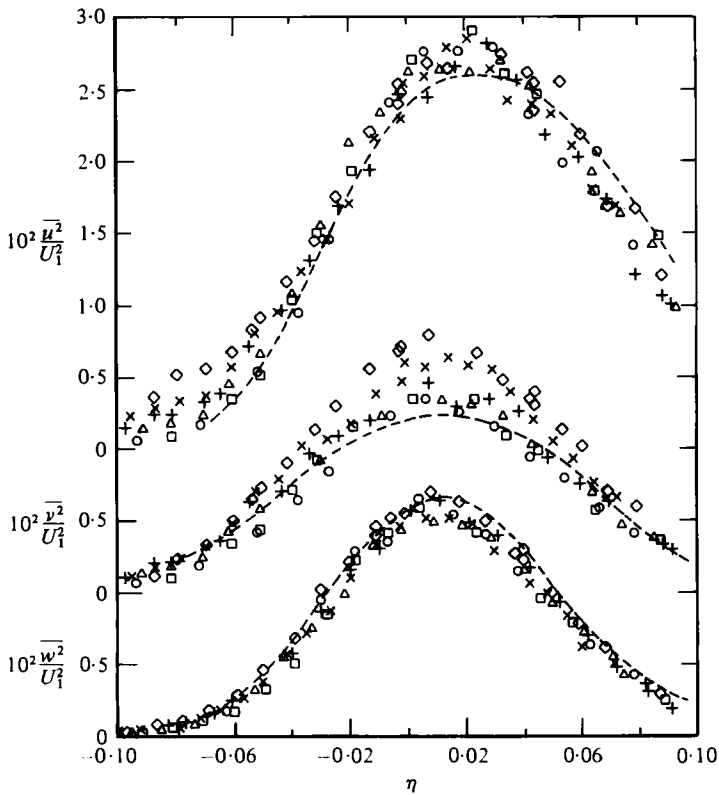

FIGURE 4. Normal-stress profiles. $\square$, $x-x_0$ (cm) $= 24\cdot05$; $\bigcirc$, $36\cdot89$; $\triangle$, $49\cdot51$; $+$, $62\cdot32$; $\times$, $75\cdot06$; $\diamond$, $100\cdot3$. Dashed line from Castro (1973), $x-x_0 = 56$ cm.
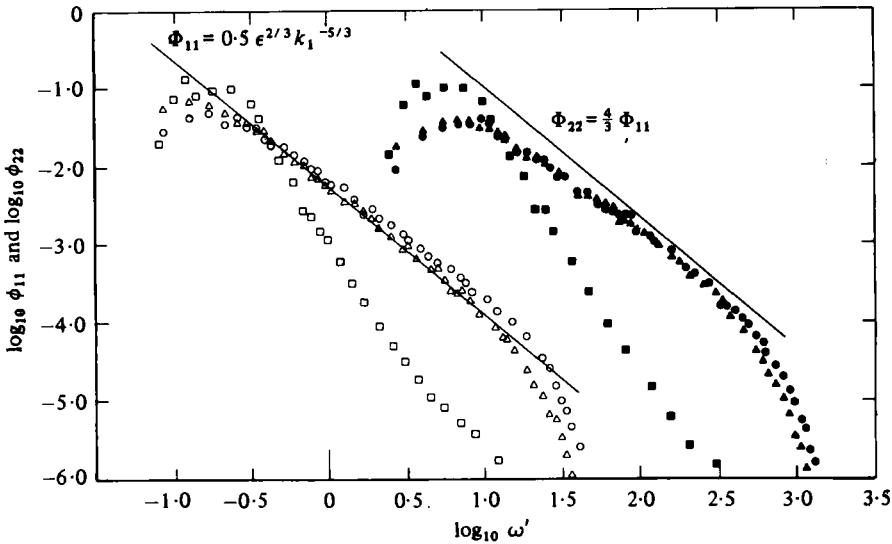
FIGURE 5. ϕ_{11} and ϕ_{22} at $x-x_0 = 36\cdot89$ cm. $\square$, $\eta = 0\cdot117$; $\bigcirc$, $-0\cdot052$; $\triangle$, $+0\cdot018$. Unfilled symbols are ϕ_{11}.

investigation we could find where $\overline{v^2}$ was measured at more than one station in a geometry similar to figure 1 was that of Wygnanski & Fiedler (1970). Their measurements were limited to the region where $\delta/h > 0\cdot8$ and do not show an increase in $\overline{v^2}$ with x. In contrast, the $\overline{w^2}$ result remain self-preserving except for a slight rise near the high-speed side (see also figure 8 of WF) which occurs for the same reason as the rise in $\overline{u^2}$.

The strongest reason for believing the rise in $\overline{v^2}$ to be at least qualitatively genuine, and not due to experimental error, is the evolution of the spectra shown in figures 5 and 6. The non-dimensional spectral density, defined as

$$\phi'_{ii}(\omega) \equiv \frac{U_1 \phi_{ii}(\omega)}{x - x_0},$$

where

$$\int_0^\infty \phi_{ii}(\omega)\, d\dot{\omega} = 1,$$

is plotted against the non-dimensional radian frequency

$$\omega' \equiv \frac{\omega(x - x_0)}{U_1}$$

for $i = 1, 2$. At 37 cm, where $\delta/h < 0\cdot8$, the spectra are unremarkable. At $\eta = +0\cdot018$, ϕ_{11} has an extensive inertial subrange and is very similar in shape to Castro's (1973) analog spectra at $\eta = 0$. Assuming that at this η convection velocity is equal to the local mean velocity and that the constant a in the inertial-subrange law

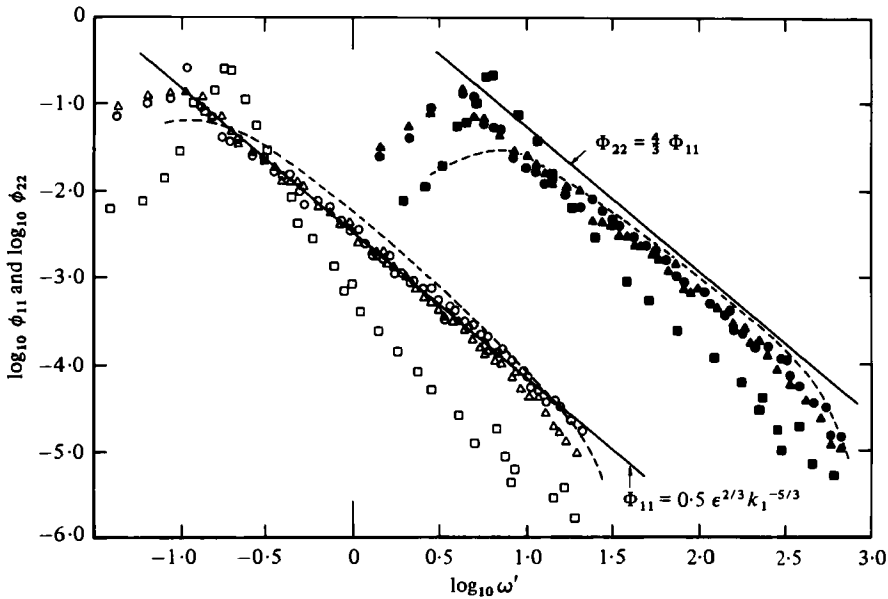$$\Phi_{11}(k_1) \equiv \overline{u^2}\phi_{11}(k_1) = a\epsilon^{\frac{2}{3}}k_1^{-\frac{5}{3}}, \tag{1}$$

FIGURE 6. ϕ_{11} and ϕ_{22} at $x - x_0 = 75 \cdot 06$ cm. $\square$, $\eta = -0 \cdot 104$; $\bigcirc$, $-0 \cdot 050$; $\triangle$, $+0 \cdot 014$. Unfilled symbols are ϕ_{11}. Dashed lines from figure 5.

where k_1 is the wavenumber and ϵ is the dissipation (strictly the energy-transfer rate), is given by $a = 0 \cdot 50$ (Townsend 1976, p. 99), we obtain a value of $0 \cdot 091 \delta$ for the dissipation length parameter $L_\epsilon \equiv (\overline{uv})^{\frac{3}{2}}/\epsilon$. This value is close to that found by Castro (1973) and to the value $L_\epsilon/\delta = 0 \cdot 10$ used in the reasonably successful calculations of WWB. Figures 5 and 6 also show the isotropic relation $\Phi_{22}(\omega) = \frac{4}{3}\Phi_{11}(\omega)$ for the inertial subrange, which is discussed further in §5.

Figure 6 shows the spectra at 75 cm with the results near maximum γ from figure 5 shown as the dashed lines; ϕ_{22} has been scaled by the ratios of $\overline{v^2}$ at 37 and 75 cm. ϕ_{11} has developed a slight peak around $\omega' = 3 \cdot 6$ and the change in ϕ_{33} (the results are not shown here) is very similar. However, the peak in ϕ_{22} near this frequency has been amplified significantly and the comparison with the results of figure 5 shows that this gain in spectral density, which is independent of η, is responsible for the rise in $\overline{v^2}$. If we assume that the convection velocity does not alter appreciably with x, then the peak in ϕ_{22} is centred around $k\delta \approx 1$. The peak wavenumber must be too large to amplify $\overline{u^2}$ by 'shaking' the mean-velocity gradient. Further discussion of $\overline{v^2}$ is delayed until §5, since we need the information about the large-eddy structure deduced from the correlation measurements in §4.

The measurements of $\overline{uv}$ are given in figure 7, together with the self-preserving distribution calculated from figure 2. The error in the measured values, about 10 %, is similar to that found in previous studies e.g. Castro (1973), Pui & Gartshore (1979) and Browand & Latigo (1979). The shear-stress correlation coefficient $R_{uv} \equiv \overline{uv}/(\overline{u^2}\,\overline{v^2})^{\frac{1}{2}}$, which is not shown here, reflects the behaviour of $\overline{v^2}$; R_{uv} reaches a maximum of $0 \cdot 52$ at 50 cm, a similar value to that found by Bradshaw, Ferriss & Johnson (1964) in an axisymmetric mixing layer, and then decreases.

The most spectacular effect of the increasing level of potential fluctuations is the evolution of the flatness factors near the high-velocity edge (figure 8). The effects of the potential fluctuations can be demonstrated as follows, using F_u as an example.
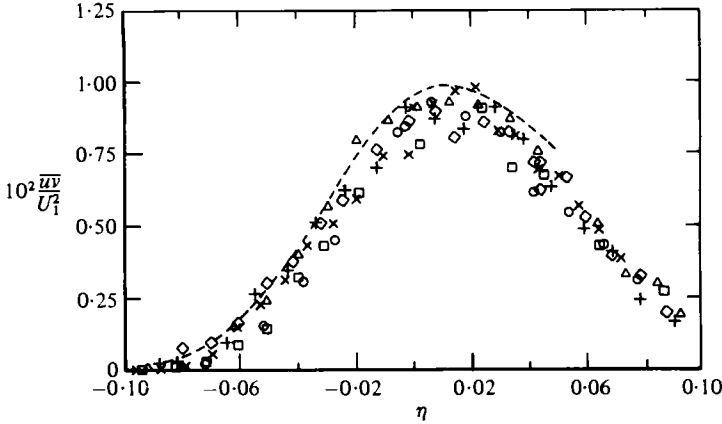
FIGURE 7. Shear-stress profiles. Symbols as in figure 4.

By definition and using the addition law, equation (A 1), we have

$$F_u \equiv \frac{\overline{u^4}}{(\overline{u^2})^2} = \frac{\gamma \overline{u_T^4} + (1-\gamma)\overline{u_N^4}}{[\gamma \overline{u_T^2} + (1-\gamma)\overline{u_N^2}]^2}. \tag{2}$$

Assuming that $\overline{u_T^4}/(\overline{u_T^2})^2 \approx 3$, which from figure 8 is a good approximation near maximum γ, and that $\overline{u_N^4}/(\overline{u_N^2})^2 \approx 3$, as in the outer potential flow (the results are not shown here), gives

$$F_u \approx 3 \frac{\gamma + (1-\gamma)(\overline{u_N^2}/\overline{u_T^2})^2}{[\gamma + (1-\gamma)(\overline{u_N^2}/\overline{u_T^2})]^2}. \tag{3}$$

There are two limits to (3), namely

$$F_u \to \frac{3}{\gamma} \quad \text{when} \quad \frac{(1-\gamma)\overline{u_N^2}}{\overline{u_T^2}} \to 0, \tag{4}$$

$$F_u \to 3 \quad \text{when either} \quad \frac{(1-\gamma)\overline{u_N^2}}{\overline{u_T^2}} \to \infty \quad \text{and} \quad \gamma \to 0 \tag{5a}$$

$$\text{or} \quad \frac{\overline{u_N^2}}{\overline{u_T^2}} \to 1. \tag{5b}$$

Equation (4) is the conventional limit, which has been widely used to estimate γ in the past. Corrsin & Kistler (1955) point out restrictions on its validity similar to those discussed here. The limit of (5a) applies to any flow for sufficiently small γ and is the reason why F_u does not increase monotonically with distance away from the flow. The importance of the limit (5b) is that F_u is independent of γ. Equations (4) and (5) are plotted in figure 8, using γ for 37 cm from figure 3. Initially F_u follows (4) more closely than does F_v, as $\overline{u^2}$ decreases more quickly than $\overline{v^2}$ with decreasing η at 37 cm. However figure 8 of WF shows that, at constant η in the potential core, $\overline{u^2}$ increases more rapidly with x than does $\overline{v^2}$, in agreement with the more rapid approach of F_u to (5) than of F_v. Although not shown here, F_w at 37 cm follows (4)
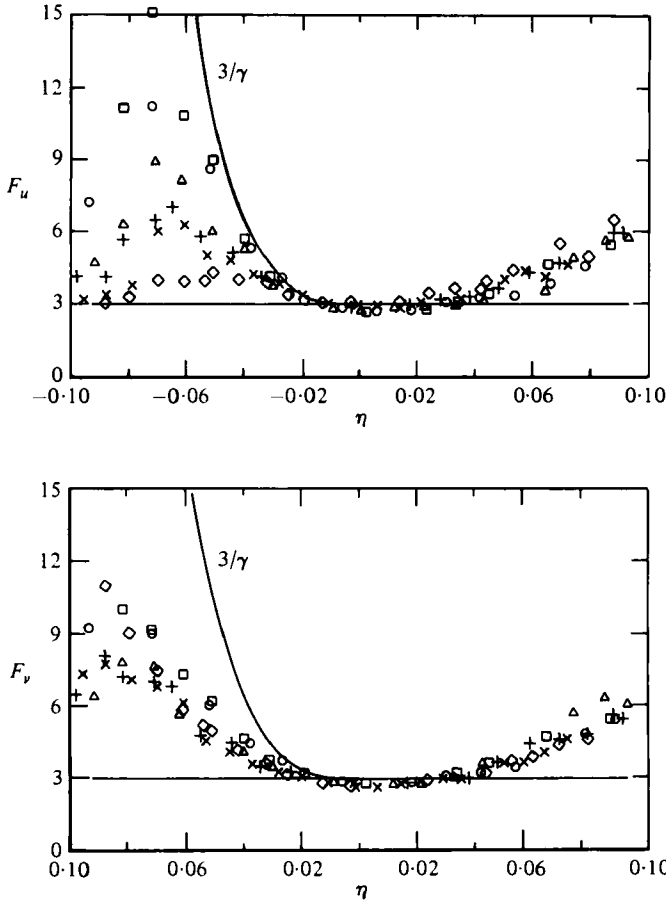
FIGURE 8. Flatness-factor profiles. Symbols as in figure 4. (a) u-component; (b) v-component.

over a larger range of η than does F_u, as $\overline{w^2}$ is the smallest of the normal stresses in the potential flow (figure 9 of WF). The decrease in F_w with increasing x is intermediate between that of F_u and F_v, as the amplification of the potential $\overline{w^2}$ is intermediate between that of $\overline{u^2}$ and $\overline{v^2}$.

The behaviour of the triple products is most conveniently described in terms of the transport velocities for the shear stress and turbulent energy. Before doing this we briefly describe the main changes in the measured triple products. Near the high-velocity edge, $\overline{u^3}$ decreases markedly in magnitude as x increases. However, $\overline{v^3}$, whose gradient appears in the diffusion term for the turbulent energy, increases in magnitude over the whole layer, as does $\overline{v^2}$. Both $\overline{u^2 v}$ and $\overline{uv^2}$ are self-preserving to within the experimental accuracy of 20%. The transport velocities for turbulent energy and shear stress are

$$V_q \equiv \frac{\overline{pv} + \tfrac{1}{2}\overline{q^2 v}}{\tfrac{1}{2}\overline{q^2}}, \quad V_\tau \equiv \frac{\overline{pu} + \overline{uv^2}}{\overline{uv}}$$

respectively, where p is the kinematic fluctuating pressure and $\overline{q^2} \equiv \overline{u^2} + \overline{v^2} + \overline{w^2}$ is twice the turbulent kinetic energy. Measurements at 37 cm showed that $\overline{w^2 v} \approx 0.20$
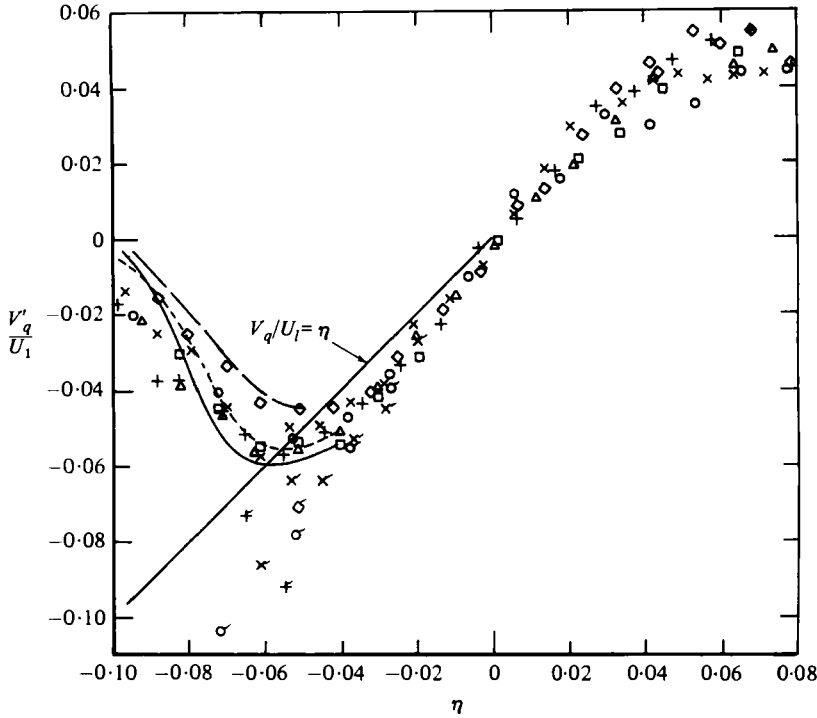
FIGURE 9. Turbulent-energy transport velocity. Symbols as in figure 4. Flagged symbols are $V'_{q,\,\mathrm{T}}$.
Equation (6b) at: ——, $x-x_0$ (cm) $= 24{\cdot}05$; ———, $62{\cdot}32$; ——, $100{\cdot}3$.

$(\overline{u^2 v}+\overline{v^3})$ to a good approximation across the whole layer. Figure 9 shows V'_q, the measured approximation to V_q, defined, neglecting the pressure term entirely, as

$$V'_q \equiv \frac{1{\cdot}2(\overline{u^2 v}+\overline{v^3})}{\overline{u^2}+\overline{v^2}+\overline{w^2}}.$$

The limiting behaviour of V'_q can be inferred from the turbulent energy equation, which reduces to advection + diffusion ≈ 0 near the high-velocity edge (see figure 23). In similarity form we have

$$(V-\eta U)\frac{\partial \overline{q^2}}{\partial \eta}+\frac{\partial \overline{q^2}V_q}{\partial \eta} \approx 0. \qquad (6a)$$

In this region $U \approx U_1$ and $V \approx 0$, so (6a) can be integrated between η_1 and η_2 to give

$$\frac{\eta \overline{q^2}}{U_1}\bigg|_{\eta_1}^{\eta_2} - \int_{\eta_1}^{\eta_2}\frac{\overline{q^2}}{U_1^2}\,d\eta \approx \frac{\eta \overline{q^2}V_q}{U_1^3}\bigg|_{\eta_1}^{\eta_2}. \qquad (6b)$$

Letting $\eta_1 \to -\infty$ shows that $V_q \to \eta U_1$ if $\overline{q^2}$ decreases sufficiently rapidly for the second term in (6b) to be negligible. It is obvious that V'_q does not tend to ηU_1 even at 24 cm; the reason is the behaviour of the second term. Equation (6b) was evaluated using both the measured $\overline{q^2}$ distribution and V'_q at the value η_2 indicated. The calculations, shown as curves in figure 9, reproduce the trend of the experimental results and justify the neglect of streamwise diffusion in (6b). The variation of V'_q with x, due to the increasing level of potential fluctuations decreasing the rate of decay of $\overline{q^2}$ near the

high-velocity edge, is much less than the change in the flatness factors. It is more difficult to interpret V_q' in terms of the addition law as there is no general simplification similar to that used in obtaining (4) and (5). Over the measured range of γ, $\overline{q^2 v_{\rm N}}$ is always much less than $\gamma \overline{q^2 v_{\rm T}}$. If we assume that $\overline{q^2 v_{\rm N}}$ is always negligible then

$$V_{q,\,{\rm T}}' \approx \gamma \overline{q^2 v_{\rm T}} / [\gamma \overline{q_{\rm T}^2} + (1-\gamma) \overline{q_{\rm N}^2}]. \tag{7}$$

Equation (7) also has two limits, namely

$$V_{q,\,{\rm T}}' \to V_q' \quad \text{when} \quad \frac{(1-\gamma) \overline{q_{\rm N}^2}}{\gamma \overline{q_{\rm T}^2}} \to 0, \tag{8a}$$

$$V_{q,\,{\rm T}}' \to \frac{V_q'}{\gamma} \quad \text{when either} \quad \frac{(1-\gamma) \overline{q_{\rm N}^2}}{\gamma \overline{q_{\rm T}^2}} \to \infty \quad \text{or} \quad \frac{\overline{q_{\rm N}^2}}{\overline{q_{\rm T}^2}} \to 1, \tag{8b}$$

where $V_{q,\,{\rm T}}' \equiv \overline{q^2 v_{\rm T}} / \overline{q_{\rm T}^2}$. The available measurements of $V_{q,\,{\rm T}}'$ are shown as the flagged symbols in figure 9. At all x, the measured $V_{q,\,{\rm T}}'$ follow ($8a$) out to $\eta \approx -0.030$, which is also the approximate limit to the validity of (4) for F_u; $\overline{u^2}$ is the largest component of $\overline{q^2}$. However, it is not possible to check the accuracy of both ($8a$) and ($8b$), particularly as V_q' is not constant.

A simplification like ($6a$) is not valid for the shear-stress transport equation near the high-velocity edge, because the pressure–strain term remains of the same order as the transport term. However, V_r should be less influenced by potential-flow effects, *not* because $\overline{uv}$ tends to zero, but because its rate of decay with decreasing η is larger than that of $\overline{q^2}$. WF show that, in general, $\overline{uv}$ is not zero in potential flow; in the present flow R_{uv} passes through zero at $\eta \approx -0.090$ and is then negative at $x > 25$ cm (figure 10 of WF). $V_r' = \overline{uv^2} / \overline{uv}$, the measured approximation to V_r, is shown in figure 10. The rapid decrease in $\overline{uv}$ makes V_r' less accurate than V_q' near the high-velocity edge and may be the explanation for the results at 100 cm, as V_r' otherwise is self-preserving. On average, the ratio V_r'/V_q' is 2·5, which is lower than the value of 3·3 found by WWB and by Smits, Young & Bradshaw (1979) in their boundary-layer measurements.

4. Two-point measurements and autocorrelations

From continuity, there can be no net flux of the fluctuating i-component velocity u_1 across the (j, k)-plane normal to the i-direction, so the covariance $\overline{u_{i,\,A} u_{i,\,B}}$ (where the subscripts A and B refer to the fixed and moving wires respectively) must integrate to zero over the (j, k)-plane. Hence the correlation must have a negative region somewhere in the plane. This negative region, which indicates 'backflow', need not occur close to either of the coordinate axes, which were the only directions of separation measured here, but the result is useful in deducing the eddy structure. The method used here to deduce the eddy structure is essentially the same as that used by Grant (1958), Bradshaw *et al.* (1964) and Townsend (1976, especially pp. 118–120). We simply look for an 'average' large-eddy shape that will explain the signs of the correlations at separations of the same order as the shear-layer thickness. The reader interested in conclusions rather than details can omit §4.1. To avoid confusion, the terms 'streamwise', 'normal' and 'spanwise' are used throughout to describe separation in the x-, y- and z-directions respectively.

WF show that the potential-core measurements at 25 cm were the only ones free of wall influence. By inference, the turbulence structure at this station was also
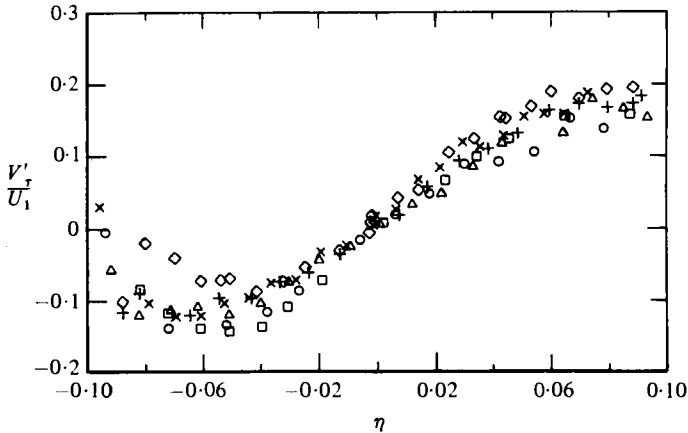
FIGURE 10. Shear-stress transport velocity. Symbols as in figure 4.

unaffected by the wall, but the mean-velocity profile was not fully developed (figure 2). The most extensive correlation measurements were made at 37 cm, the station considered to give the best compromise between the approach to full development and the onset of wall effect. The results of §3 show that the differences in the single-point results between 24 and 37 cm are small. Furthermore, the detailed correlation measurements at 24 cm, given in Wood (1980) but not here, show no significant differences from those at 37 cm when the non-dimensional separation $r/(x-x_0)$ is used. It is concluded that the correlation measurements at 37 cm are representative of a fully developed mixing layer in the absence of wall effect. With the exception of $\overline{v^2}$, the wall effect on the single-point results occurs only on the high-velocity side, so the correlation measurements were limited to $\eta \leqslant +0.025$.

4.1. *Correlations in the absence of wall effect* ($x = 37$ mm)

These are presented in the order 'spanwise' (z), 'normal' (y) 'streamwise' (x) (i.e. $(0, 0, r)$, $(0, r, 0)$ and $(r, 0, 0)$ respectively in the usual notation for correlation separations), followed by the intermittency correlations and the conditionally sampled ('spanwise') correlations.

For $\eta \geqslant -0.040$, $R_{11}(0, 0, r)$ (figure 11) has a negative loop that varies little in position or size, the most negative value being about -0.10; for $\eta \leqslant -0.051$, $R_{11}(0, 0, r)$ is always positive and the scale increases rapidly with decreasing η. Townsend's (1976) definition of correlation scale is used here; it is either the position of $R_{ij} = 0.05$ if R_{ij} is always positive, or the crossover point after the negative region, if any. The spanwise scales in the high-intensity region are 0.6δ for $R_{11}(0, 0, r)$ and 1.5δ for $R_{22}(0, 0, r)$ (figure 12). The latter correlation is always positive but its increase in scale with decreasing η (and γ) is less than that for $R_{11}(0, 0, r)$. Figure 13 shows that $R_{12}(0, 0, r)$, which is equal to $R_{21}(0, 0, r)$ in two-dimensional flows, is similar to $R_{11}(0, 0, r)$. $R_{33}(0, 0, r)$ (figure 14), has a negative region even though it is a 'longitudinal' correlation. In the high-intensity region the negative peak is about -0.05. The crossover point moves outward with decreasing η and the negative peak increases in magnitude, reaching -0.14 in the potential flow, as indicated on figure 14.

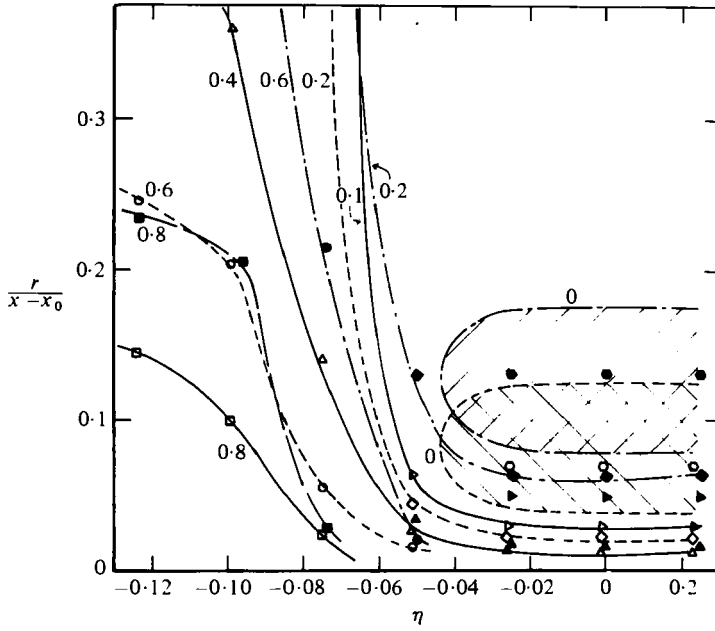As an example of the normal correlations, $R_{11}(0, r, 0)$ is shown in figure 15, with

FIGURE 11. Contour plot of $R_{11}(0, 0, r)$ at $x-x_0$ (cm) $= 36{\cdot}41$ (unfilled) and $77{\cdot}64$ (filled). $\square$, $R_{11}(0, 0, r) = 0{\cdot}8$; $\bigcirc$, $0{\cdot}6$; $\triangle$, $0{\cdot}4$; $\diamondsuit$, $0{\cdot}2$; $\triangleright$, $0{\cdot}1$. Negative region is shaded. R is defined in (A 3). $\bigcirc$, Minima at $36{\cdot}41$ cm ($\approx -0{\cdot}01$); $\bullet$, minima at $77{\cdot}64$ ($\approx -0{\cdot}04$).
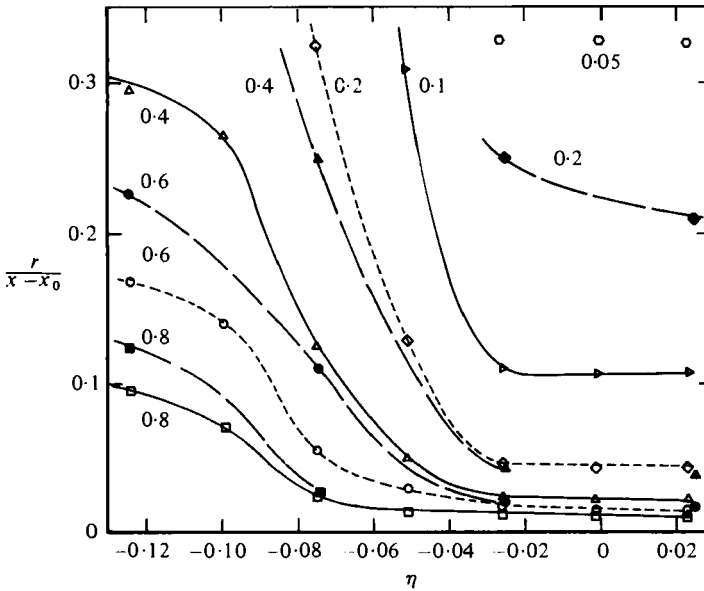
FIGURE 12. Contour plot of $R_{22}(0, 0, r)$ at $x-x_0$ (cm) $= 36{\cdot}41$ and $77{\cdot}64$. Symbols as in figure 11, except $\bigcirc = 0{\cdot}05$.
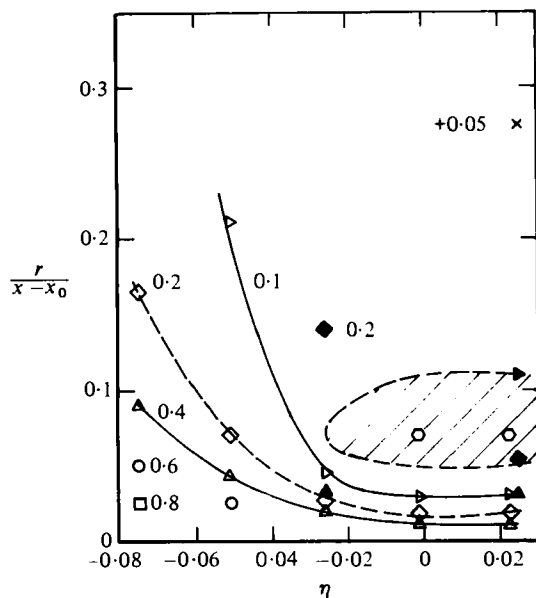
FIGURE 13. Contour plot of $R_{12}(0, 0, r)$ at $x-x_0$ (cm) $= 36\cdot41$ and $77\cdot64$. Symbols and shading as in figure 11. ◯, Minima at $36\cdot41$ cm ($= -0\cdot01$). $\times = +0\cdot05$ at $77\cdot64$ cm only.
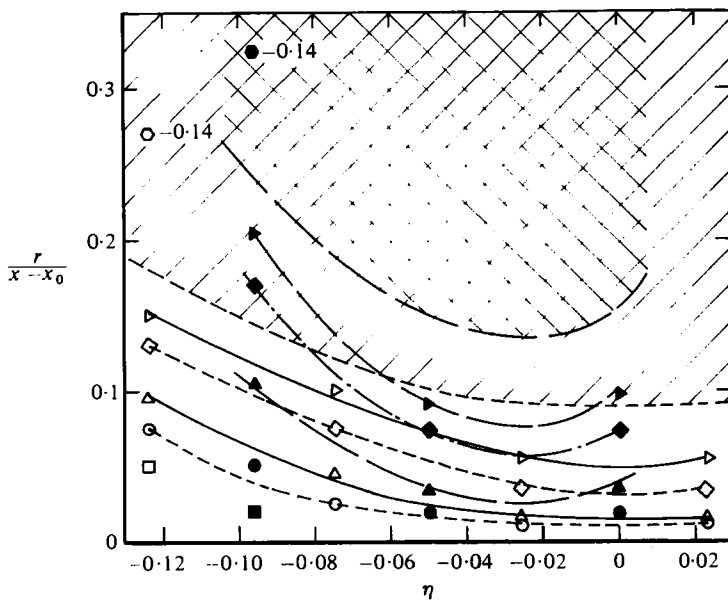

FIGURE 14. Contour plot of $R_{33}(0, 0, r)$ at $x-x_0$ (cm) $= 36\cdot41$ and $77\cdot64$. Symbols and shading as in figure 11.
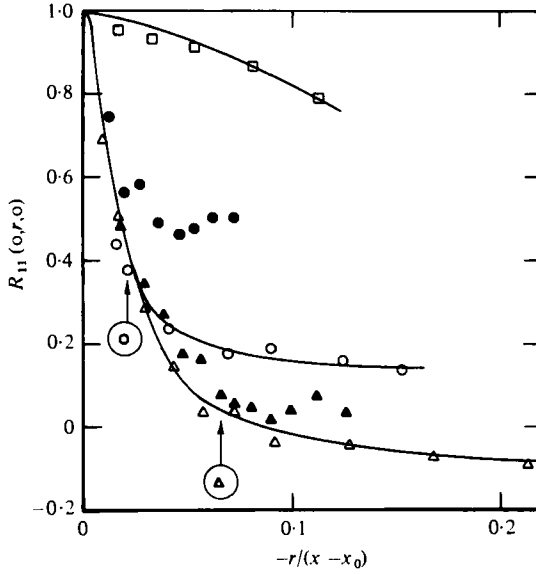
FIGURE 15. $R_{11}(0, r, 0)$. $x-x_0 = 36\cdot89$ cm: $\square$, $\eta = -0\cdot099$; $\bigcirc$, $-0\cdot049$; $\triangle$, $+0\cdot033$. $x-x_0 = 75\cdot14$ cm: $\bullet$, $\eta = -0\cdot050$; $\blacktriangle$, $+0\cdot003$. Arrows indicate edge of shear layer.

η	$R_{11}(r', 0, 0)$			$R_{22}(r', 0, 0)$			$R_{33}(r', 0, 0)$		
	(a)	(b)	(c)	(a)	(b)	(c)	(a)	(b)	(c)
				$x-x_0 = 36\cdot89$ cm					
−0·117	0·160	0·280	−0·31	0·160	0·270	−0·34			
−0·109							0·155	0·260	−0·26
−0·063							0·110	0·195	−0·09
−0·052	0·160	0·310	−0·08	0·120	0·260	−0·11			
+0·016							0·085	0·170	−0·08
+0·018	0·195	0·430	−0·07	0·120	0·187	−0·08			
				$x-x_0 = 75\cdot06$ cm					
−0·108							0·175	0·305	−0·35
−0·104	0·180	0·330	−0·55	0·155	0·310	−0·47			
−0·052							0·250	0·480	−0·09
−0·050	0·370	0·720	−0·21	0·300	0·580	−0·26			
+0·014	0·320	0·570	−0·13	0·255	0·530	−0·23	0·210	0·350	−0·09

TABLE 1. Properties of 'streamwise' correlations. Values are $r'/(x-x_0)$, where $r' = U_c t$ at (a) crossover point and (b) position of negative peak. (c) is *value* of negative peak.

the position of the fixed probe indicated. The vertical lines indicate the shear-layer edge, defined as the value of η for which $U = 0\cdot995U_1$. Of the normal correlations not shown, $R_{22}(0, r, 0)$ is always positive and of larger scale than $R_{11}(0, r, 0)$ for the fixed probe at $\eta = +0\cdot03$ and $-0\cdot049$. $R_{33}(0, r, 0)$ is always positive, but $R_{21}(0, r, 0)$ is consistently negative when the moving probe is in the potential flow, although the accuracy of measurement is obviously low.

The autocorrelations, generated from the spectra shown in figures 5 and 6, were
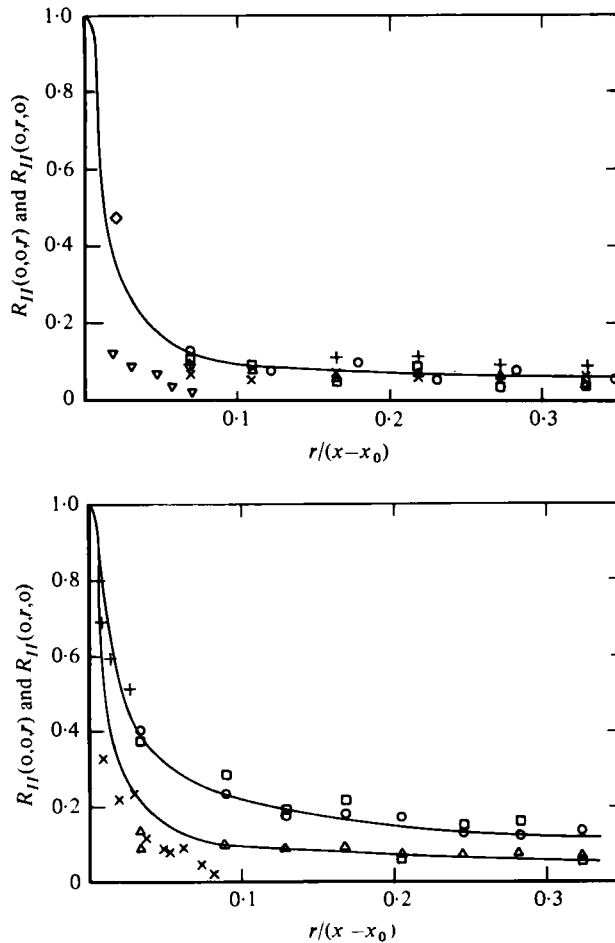
Figure 16. $R_{II}(0, 0, r)$ and $R_{II}(0, r, 0)$; see equation (A 6) for definition. (a) Nominal $x - x_0 = 36$ cm. $R_{II}(0, 0, r)$: $\square$, $\eta = -0.075$; $\bigcirc$, -0.051; $\triangle$, -0.026; $+$, -0.01; $\times$, $+0.023$. $R_{II}(0, r, 0)$: $\diamondsuit$, $\eta = -0.049$; $\triangledown$, $+0.002$. Note that r is negative for correlations in y-direction. (b) Nominal $x - x_0 = 75$ cm. $R_{II}(0, 0, r)$: $\square$, $\eta = -0.074$; $\bigcirc$, -0.025; $\triangle$, $+0.025$. $R_{II}(0, r, 0)$: $+$, $\eta = -0.050$; $\times$, $+0.003$.

converted into pseudo-streamwise correlations by using $r' = U_c t$, where U_c is the convection velocity and t is the time delay. On the basis of the convection velocities measured by Bradshaw *et al.* (1964) and Wills (1964), U_c was assumed to be either $U(\eta)$ for $\eta > 0$ or $U(\eta = 0)$ for $\eta \leqslant 0$ for all components. These assumptions are somewhat arbitrary, especially since we are unaware of any U_c measurements for the w-component, but the conclusions based on the 'streamwise' correlations are not sensitive to the precise value of U_c. At both 37 and 75 cm all the 'streamwise' correlations have negative regions, as would be expected from figures 5 and 6, emphasizing both the strong streamwise periodicity of the large eddies and that most of the backflow for v and w occurs on the x-axis. The position of the first crossover point and the position and size of the negative peak are given in table 1.

The spanwise and normal correlations of the intermittency function (A 6) are shown in figure 16. The spanwise scale varies remarkably little with η and is nearly equal
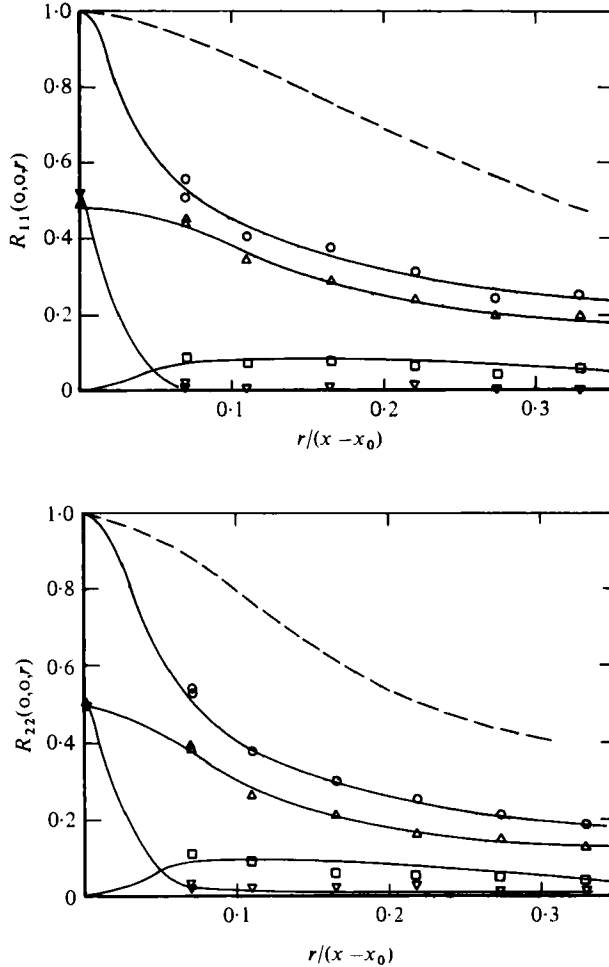
FIGURE 17. Conditionally sampled spanwise correlations. $x - x_0 = 36 \cdot 14$ cm, $\eta = -0 \cdot 075$. $\bigcirc$, Total correlation; $\triangledown$, turbulent/turbulent (TT) contribution; $\triangle$, non-turbulent/non-turbulent (NN); $\square$, TN + NT. Dashed line is total correlation at $\eta = -0 \cdot 124$. (a) $R_{11}(0, 0, r)$; (b) $R_{22}(0, 0, r)$.

to the scale of $R_{22}(0, 0, r)$ in the high-intensity region, suggesting that the increase in scale of $R_{11}(0, 0, r)$, $R_{22}(0, 0, r)$ and all the single-component normal correlations for decreasing η, is caused by the effects of the potential flow. The theoretical support for this statement is discussed in WF.

Using the conditional sampling routines described in the appendix, the contributions to the total correlations were found (figures 17–20). The non-turbulent/turbulent (NT) and turbulent/non-turbulent (TN) contributions, which are nominally equal for spanwise separations, are shown together for clarity. At 37 cm the most spectacular results, for $\eta = -0 \cdot 075$ (figure 17), show conclusively that *the dominant contribution at large separations is from the potential* (*NN*) *motion*. The scales of the turbulent (TT) motion are no larger than the scales of the *total* correlations in the high-intensity region for both $R_{11}(0, 0, r)$ and $R_{22}(0, 0, r)$. Unusually there is no negative loop in the TT contribution to $R_{11}(0, 0, r)$, which is probably genuine in view of the similarity in
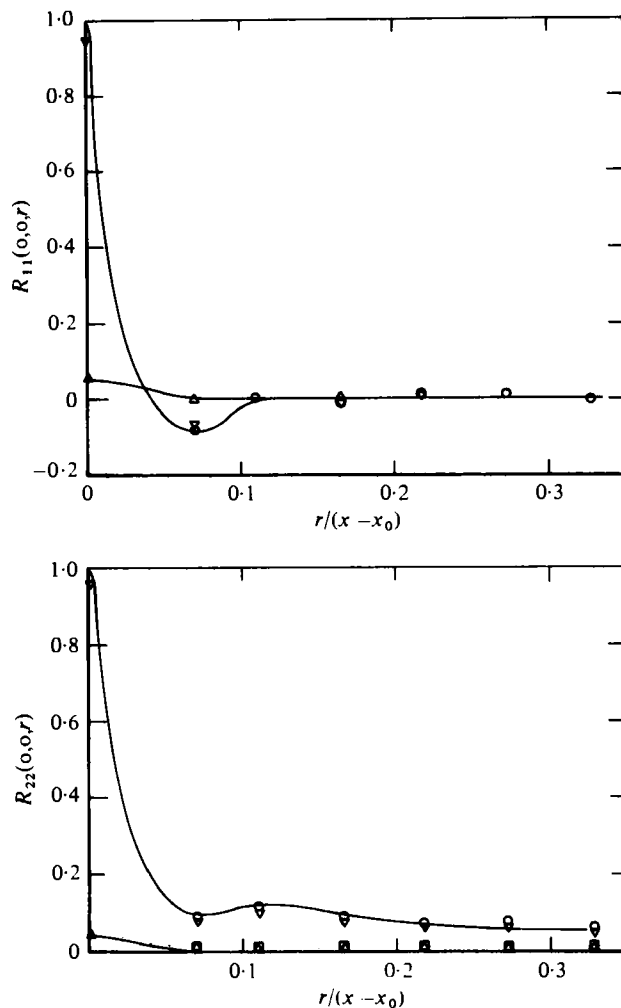
FIGURE 18. Conditionally sampled spanwise correlations. $x - x_0 = 36\cdot41$ cm, $\eta = +0\cdot023$. Symbols as in figure 17. (a) $R_{11}(0, 0, r)$; (b) $R_{22}(0, 0, r)$.

shape of the NN contribution and the *total* (potential) correlation at $\eta = -0\cdot124$, which is also shown in figure 17. Of the other results (see Wood 1980) the TT contribution to $R_{11}(0, 0, r)$ at $\eta = -0\cdot051$ is still positive, while all three contributions to $R_{22}(0, 0, r)$ are roughly equal. About half of the negative loop in $R_{11}(0, 0, r)$ at $\eta = -0\cdot026$ is due to the turbulent motion, the rest being the sum of the NT and TN contributions. The contributions to $R_{22}(0, 0, r)$ at $\eta = -0\cdot026$ and $-0\cdot01$ and to $R_{11}(0, 0, r)$ at $\eta = -0\cdot01$ are very similar to those at $\eta = +0\cdot023$, shown in figure 18. As expected, nearly all the total correlation at $\eta = +0\cdot023$, including the negative loop in $R_{11}(0, 0, r)$, is due to the turbulent motion. Although not shown, the general similarity between $R_{11}(0, 0, r)$ and $R_{12}(0, 0, r)$ extends to the respective contributions, except that the sums of the NT and TN contributions to $R_{12}(0, 0, r)$ are small and negative for large separation at $\eta = -0\cdot051$ and $-0\cdot026$.

The major difference between the present spatial correlations at 37 cm and the
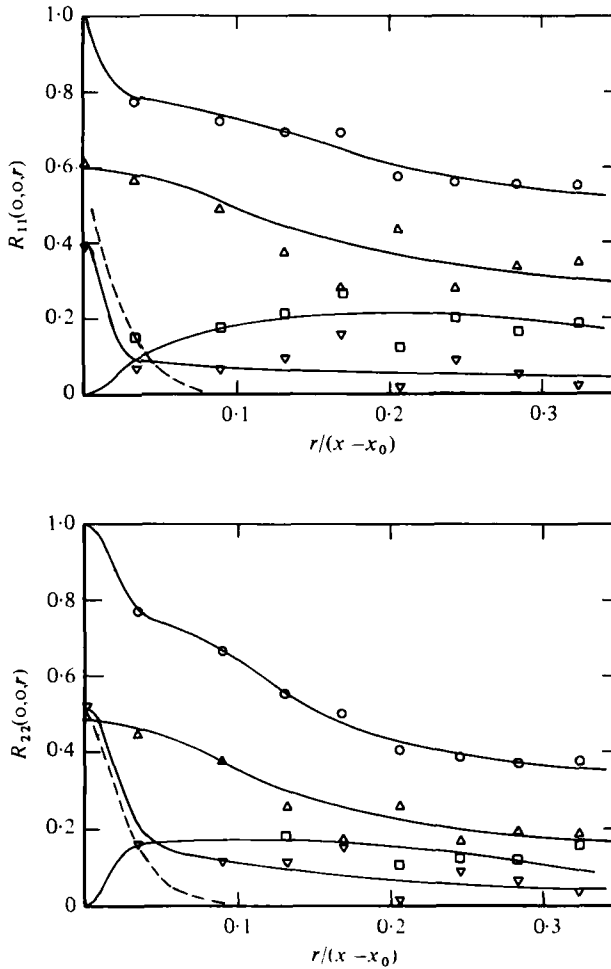
FIGURE 19. Conditionally sampled spanwise correlations. $x - x_0 = 77.64$ cm, $\eta = -0.074$. Symbols as in figure 17. Dashed line is TT from figure 17. (a) $R_{11}(0, 0, r)$; (b) $R_{22}(0, 0, r)$.

axisymmetric results of Bradshaw *et al.* (1964) and Weber (1974) is the negative region in the present $R_{33}(0, 0, r)$. This negative region appears even in the high-intensity region, where the potential contribution to both $R_{11}(0, 0, r)$ and $R_{22}(0, 0, r)$ is negligible (figure 18), and so is due to the turbulent motion. Since the spanwise scale of the turbulent motion does not increase with decreasing η, the outward movement of the crossover point in $R_{33}(0, 0, r)$ with decreasing η is due to the potential motion. Bradshaw *et al.* (1964) suggested that the negative loop in $R_{11}(0, 0, r)$ was 'associated with the v-motion rather than the w-motion' largely because the negative peak in their $R_{11}(0, 0, r)$ decreased by a similar amount to the decrease in the peak of ϕ_{22} as x increased. In the present flow the negative loop in $R_{11}(0, 0, r)$ decreased in magnitude and moved outward (compare figures 17 and 18), while ϕ_{22} has developed a strong peak (figure 6). Thus it is not possible to interpret the present correlations exclusively in terms of Grant's (1958) mixing jets, which Bradshaw *et al.* (1964) considered were the dominant eddy structure in their flow.
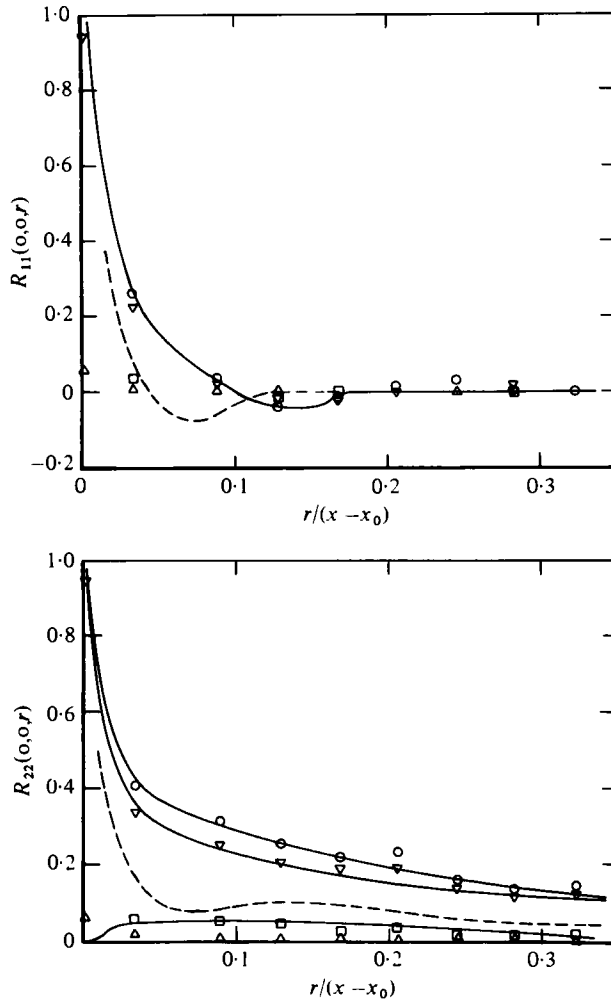
FIGURE 20. Conditionally sampled spanwise correlation. $x - x_0 = 77.64$ cm, $\eta = +0.025$. Symbols as in figure 17. Dashed line is TT from figure 18.

4.2. *Large-eddy structure in the absence of wall effect*

The most economical interpretation of the present spatial correlations, although not the only one, is that the large eddies are horseshoe vortices or hairpin eddies as shown in figure 21 (*a*). In the high-intensity region, where $R_{11}(0, 0, r)$ has a negative loop, the horseshoe vortex looks like Grant's (1958) double-roller eddy whose circulation is confined almost exclusively to the (x, z)-plane. This structure causes the negative loops in $R_{11}(0, 0, r)$ and $R_{33}(0, 0, r)$; Grant considered the latter to be the strongest evidence for double-roller eddies. Superimposed on this structure is an 'outward' motion, away from the high-intensity region, primarily responsible for the $R_{22}(0, 0, r)$ results. The reasons for assuming this superposition are (i) the striking similarity between $R_{11}(0, 0, r)$ and $R_{12}(0, 0, r)$; (ii) the fact that the scale of the turbulent contribution to $R_{11}(0, 0, r)$ is nearly half that to $R_{22}(0, 0, r)$; and (iii) the fact that,
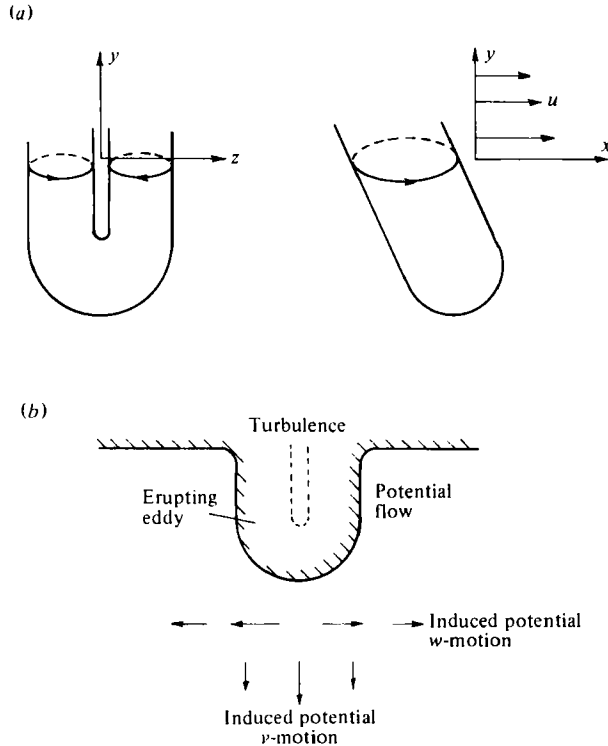
(a)

(b)

FIGURE 21. (a) Schematic diagram of horseshoe eddy. (b) Effect on potential flow.

although not shown here, the scale of the turbulent contribution to $R_{22}(0, r, 0)$ exceeds that to the other normal correlations.

The outward motion joins the vortex lines of the double-roller eddy and removes the negative loop in the turbulent contribution to $R_{11}(0, 0, r)$, (and, presumably, to $R_{33}(0, 0, r)$ as well) as the circulation is altered to the (x, y)-plane. The role of the outward motion is similar to that ascribed, by Grant, to the mixing jets; in his turbulent cylinder wake he found that $R_{22}(0, 0, r)$ was always positive and had a scale that was independent of y.† However, there are at least three indications that the eddy structure is not as simple as implied above, all related to the fact that the circulation in the double-roller eddy, as conceived by Grant, is confined almost entirely to the (x, z)-plane. Thus the motion at any position y within the eddy cannot provide backflow for the u- or w-motion at any other y. Firstly, this restriction implies that

$$\int_0^\infty R_{11}(0, 0, r)\, dr = \int_0^\infty R_{33}(r, 0, 0)\, dr = 0,$$

which is not consistent with either the present results (obviously the autocorrelation of ϕ_{33} must have a non-zero integral scale) or those of Grant. Secondly, $R_{11}(0, 0, r)$

† For the reasons given in WF, potential-flow effects are smaller in wakes than in mixing layers. Briefly, the faster growth of a mixing layer means that a variation in the non-dimensional normal coordinate, η for a mixing layer, corresponds to a larger variation in y (which scales the potential correlations) for a mixing layer than it does for a wake.

and $R_{11}(0, r, 0)$ are always positive when both probes are in the potential flow, and the analysis of WF suggests that the turbulent regions supply some of the backflow for the potential u-motion. Thirdly, an eddy structure with only y-component vorticity cannot contribute directly to $\overline{uv}$ and so is not of primary importance.

The large-eddy structure must be inclined, in the (x, y)-plane, as shown in figure 21 (*a*), to extract energy from the mean flow efficiently. Assuming that the crossover point in $R_{33}(r', 0, 0)$ is the radius of the average double-roller eddy gives a rough estimate of its streamwise scale as 0.9δ from table 1. Note that the double-roller structure is consistent with the crossover point for $R_{33}(r', 0, 0)$ being the smallest of the three 'streamwise' correlations, but is not consistent with the negative region in $R_{11}(r', 0, 0)$ for $\eta = +0.018$. This discrepancy could be due to the lack of simple superposition or to the inevitable low-wavenumber v-motion, which can contribute to the u-motion via the mean-velocity gradient, which is a maximum near $\eta = +0.018$. Obviously this 'flapping' motion could *not* be responsible for the negative region in $R_{11}(0, 0, r)$, which occurs at lower values of r than the crossover point in table 1. For all η, the backflow for v occurs at least partially along the x-axis; near maximum γ this is probably achieved by the alternative dispatch of 'outward' fluid to the high- and low-velocity sides, as the turbulent eddies erupt into the potential flow.

The effect of such an eruption on the potential flow is shown schematically in figure 21 (*b*). Since the $R_{II}(0, 0, r)$ results give no indication of spanwise periodicity in the large-eddy structure, an explanation in terms of one eddy alone is justified. In the (x, y)-plane the eddy 'pushes' the potential flow away from the eddy centre, causing positive contributions to the potential $R_{22}(0, 0, r)$ and contributions to $R_{33}(0, 0, r)$ of opposite sign at an r depending on y. This is consistent with $R_{22}(0, r, 0)$ for the fixed probe in the high-intensity region, which is the largest of the normal correlations. The corresponding $R_{33}(0, r, 0)$ is positive because the w-motion at the downstream edge of the eddy is away from the eddy centre, as is the potential motion. As the eddy moves downstream and/or decays, the potential motion moves inward to fill the gap, producing contributions to the correlations of the same sign as discussed above. Since the convection velocity of the large eddy is less than U_1, it represents a blockage to the potential flow. This causes positive contributions to the potential $R_{11}(0, 0, r)$ and $R_{11}(0, r, 0)$ both when the eddy is in the plane of interest, and the potential u is accelerated, and after the eddy has moved downstream and the potential flow decelerates. Illustration of this 'blockage' effect on the potential motion is provided by Yule (1978, figure 11) and the study, by Van Atta *et al.* (1982), of potential flow above a turbulent spot in a laminar boundary layer. WF discuss the theoretical aspects of the potential flow by an extension of the analysis of Phillips (1955).

4.3. *Correlation and large-eddy structures in wall effect* ($x = 75$ mm)

Firstly, we show that the changes in the correlations evident from figures 11–14 are indeed caused by wall effect and are not due to some peculiarity of the chosen measurement station. If only wall effect changes the correlations, then the only possibility for scaling the correlations, using $R_{11}(0, 0, r)$ as an example, is

$$R_{11}(0, 0, r) = f[r/(x - x_0), \eta, \eta_{\mathrm{w}}], \tag{9}$$

where f denotes functional dependence and η_{w} is the position of the wall in similarity coordinates. The results at 37 cm are for η_{w} of sufficient magnitude to be negligible.
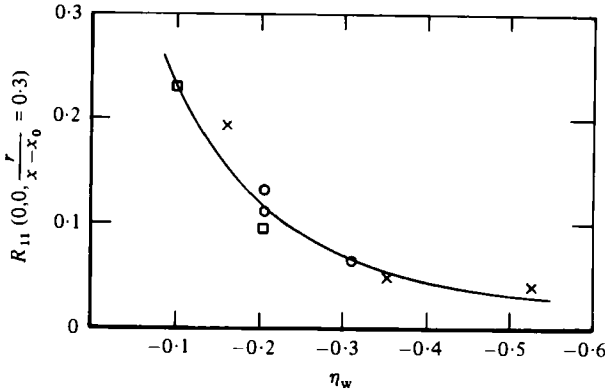
FIGURE 22. Experimental test of (9); $\eta = -0\cdot050$. Analog results: $\bigcirc$, no false floor; $\square$, with false floor. Digital results from figure 11: $\times$, no false floor.

Before the final measurements were started, (9) was tested by inserting a false floor, parallel to the wind-tunnel floor, to vary η_w independently of x. $R_{11}(0, 0, r)$ was measured using analog equipment and both these results and the later, digital results for $r/(x-x_0) = 0\cdot30$ and $\eta = -0\cdot050$ are shown in figure 22 to support (9).

Dimensionless scales of the normal correlations have increased at 75 cm, as can be seen in figure 15 for $R_{11}(0, r, 0)$; the other correlations are not presented. This increase is due largely to an increase in the TN contribution, as the 'blockage' effect is more pronounced at 75 cm, while the turbulent contributions have not altered significantly.

The negative peak in $R_{11}(0, 0, r)$ (figure 11) has decreased in size to about $-0\cdot04$, and the crossover point in both $R_{11}(0, 0, r)$ and $R_{33}(0, 0, r)$ (figure 14) has moved to larger r. The change in the streamwise correlations reflects the change in the spectra (figures 5 and 6). Table 1 shows that values of r' at the crossover points in all the measurements have increased by a factor of about two, which is more than could be plausibly attributed to a change in the convection velocity. These results are consistent with the proposed eddy structure of the unaffected flow (figure 21a). As the x- and z-scales of the double roller eddy are stretched by wall effect, the y-component vorticity is decreased.

$R_{12}(0, 0, r)$ (figure 13) is no longer similar to $R_{11}(0, 0, r)$ and $R_{II}(0, 0, r)$ (figure 16b) has significantly increased for $\eta \leqslant -0\cdot025$. Figure 19 shows that all the contributions to both $R_{11}(0, 0, r)$ and $R_{22}(0, 0, r)$ have increased near the high-velocity edge. The increase in the total correlations at $\eta = +0\cdot025$ (figure 20) and $\eta = -0\cdot026$ (the results are not shown) is due largely to the increased turbulent contribution.

In summary, the double-roller component of the large-eddy structure has been weakened by the effect of the wall, and this presumably increases the importance of the outer motion. The scales of the $(0, r, 0)$ correlations have increased, largely because of the increase in the TN contributions, while *all* the conditionally sampled spanwise measurements show an increase in the turbulent contribution. It is difficult to see how this could occur if the unaffected large-eddy structure was essentially two-dimensional, as suggested by e.g. Roshko (1976).

5. General discussion

This paper is not intended as a treatment of empirical turbulence models, but the discussion below is applicable to turbulence models based on term-by-term modelling of the Reynolds-stress transport equations, and especially to the representation of wall effect, for which an extra correction term is needed in many models.

With some knowledge of the large-eddy structure it is possible to explore further the behaviour of the normal stresses, in particular the change in ϕ_{22} across the whole layer for $x - x_0 > 50$ cm. From the discussion of §4, this rise must be associated with the nature of the outward motion. We begin by showing that the behaviour of $\overline{v^2}$ can be explained plausibly in terms of the thin-shear-layer equations for the normal stresses and so is *not* due to any sort of upstream influence. These equations are

$$U\frac{\partial \frac{1}{2}\overline{u^2}}{\partial x} + V\frac{\partial \frac{1}{2}\overline{u^2}}{\partial y} + \overline{uv}\frac{\partial U}{\partial y} + \overline{u^2}\frac{\partial U}{\partial x} - \overline{p\frac{\partial u}{\partial x}} + \frac{\partial \frac{1}{2}\overline{u^2 v}}{\partial y} + \epsilon_u = 0, \qquad (10a)$$

$$U\frac{\partial \frac{1}{2}\overline{v^2}}{\partial x} + V\frac{\partial \frac{1}{2}\overline{v^2}}{\partial y} - \overline{v^2}\frac{\partial U}{\partial x} - \overline{p\frac{\partial v}{\partial y}} + \frac{\partial}{\partial y}(\overline{pv} + \tfrac{1}{2}\overline{v^3}) + \epsilon_v = 0, \qquad (10b)$$

$$U\frac{\partial \frac{1}{2}\overline{w^2}}{\partial x} + V\frac{\partial \frac{1}{2}\overline{w^2}}{\partial y} - \overline{p\frac{\partial w}{\partial z}} + \frac{\partial \frac{1}{2}\overline{w^2 v}}{\partial y} + \epsilon_w = 0. \qquad (10c)$$

Summing these equations gives the turbulent-energy equation

$$U\frac{\partial \frac{1}{2}\overline{q^2}}{\partial x} + V\frac{\partial \frac{1}{2}\overline{q^2}}{\partial y} + \overline{uv}\frac{\partial U}{\partial y} + (\overline{u^2} - \overline{v^2})\frac{\partial U}{\partial y} + \frac{\partial}{\partial y}(\overline{pv} + \tfrac{1}{2}\overline{q^2 v}) + \epsilon = 0; \qquad (10d)$$

that is

ADVECTION + PRODUCTION + DIFFUSION + DISSIPATION = 0.

Here ϵ_u is the u-component of the dissipation ϵ, and similarly for ϵ_v and ϵ_w. If the dissipation is isotropic then $\epsilon_u = \epsilon_v = \epsilon_w = \frac{1}{3}\epsilon$. The terms $\overline{p\,\partial u_i/\partial x_i}$, where p is the kinematic fluctuating pressure, are 'redistribution' terms, since they sum to zero by continuity. The balance of the terms, in mixing-layer similarity form, of $(10d)$ is shown in figure 23 for the substantially self-preserving flow at 50 cm and the wall-affected flow at 75 cm. The shear-stress values used were those calculated from the momentum equation and shown in figure 7, the approximation for $\overline{q^2 v}$ was the same as that used in V'_q, and the dissipation was found by difference. The normal-stress production was always less than 5 % of the shear-stress production for $\eta \leqslant +0.030$, rising to 15 % at $\eta = +0.060$ at 50 cm. The change in the total production with x is negligible. At 50 cm the dissipation is in reasonable agreement with the relation $\epsilon = 10(\overline{uv})^{\frac{3}{2}}/\delta$ mentioned in §3. While the agreement between the dissipation found by difference and that obtained from the inertial-subrange equation, (1), is only fair at both stations, the indicated decrease between the stations is in much better agreement.

Some of the disagreement between the two methods of obtaining the dissipation can be attributed to the uncertainty in choosing a convection velocity. Taking $U_c = U(\eta = 0)$ would give virtually no disagreement, while leaving the indicated decrease largely unaltered from that shown in figure 23. Thus, provided that the convection velocity has not significantly altered between 50 and 75 cm, the indicated
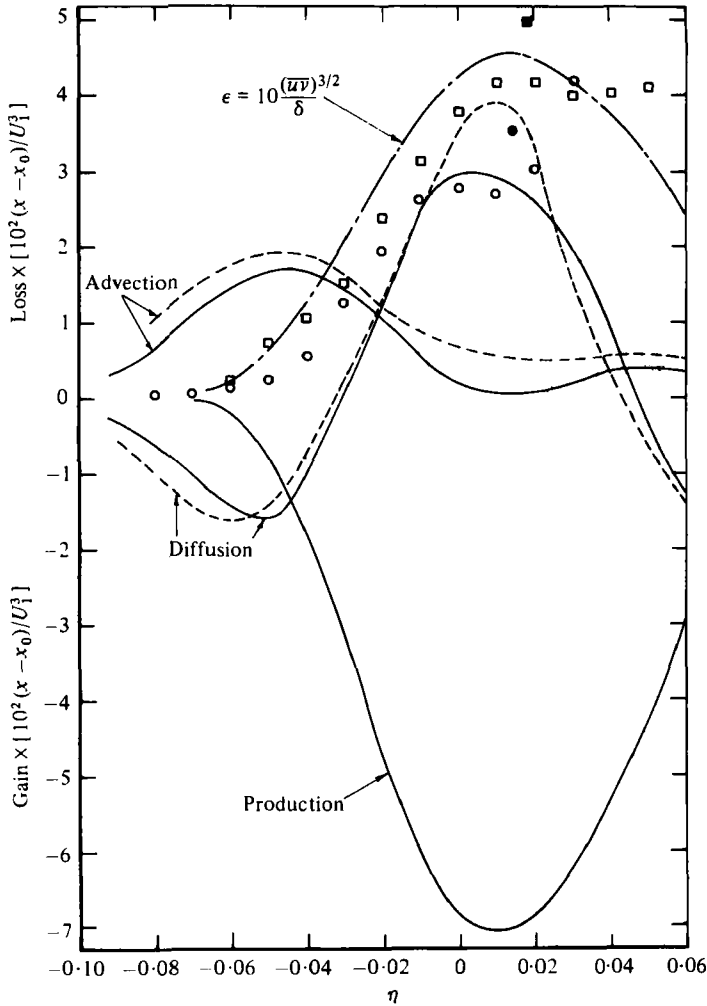
FIGURE 23. Balance of turbulent-energy equation. Solid lines, $x-x_0$ (cm) = 49·51; dashed lines, 75·06. Dissipation by difference at: $\square$, $x-x_0$ (cm) = 49·51; $\bigcirc$, 75·06. Dissipation from (1): $\blacksquare$, $x-x_0$ (cm) = 36·89; $\bullet$, 75·06.

decrease is probably more accurate than the actual values of dissipation at either station.

Equation (1) is almost independent of the details of the low-wavenumber end of the spectrum and hence of the accuracy of (10*d*) so this result implies that (10*d*) describes the flow adequately, provided that the convection velocity is not significantly altered. Therefore it is unlikely that the rise in $\overline{v^2}$ is due to any significant upstream influence.

Neither the diffusion terms in the equations for the normal stresses nor $\overline{v^2}\partial U/\partial x$, the direct production of $\overline{v^2}$, could produce a rise in ϕ_{22} across the *whole* layer. This rise must be due to the effect of the wall on the pressure field, since pressure disturbances are the only perturbations that can propagate vertically in a thin shear layer. The wall apparently alters the redistribution terms in (10); $\overline{p\partial u/\partial x}$, which generally must be negative to produce a source for $\overline{v^2}$ and $\overline{w^2}$, decreases further and

this decrease is absorbed by $\overline{p\,\partial v/\partial y}$. The reduction in $\overline{p\,\partial u/\partial x}$ in turn reduces the amount of u-component energy available for transfer to higher wavenumbers, causing ϵ_u to decrease but leaving the level of $\overline{u^2}$ largely unchanged. Apparently there is no corresponding rise in ϵ_v as $\overline{p\,\partial v/\partial y}$ increases, because the isotropic relation for the inertial subrange, Φ_{22}, $\Phi_{33} = \frac{4}{3}\Phi_{11}$, is only a slightly poorer fit to the data at 75 cm (figure 6) than at 37 cm (figure 5). All of ϵ_u, ϵ_v and ϵ_w appear to have decreased by a similar amount, as would be expected if the dissipation was nearly isotropic, causing the 'banking up' of ϕ_{22}, and to a lesser extent of ϕ_{11} and ϕ_{33}, around $k\delta \approx 1$ at 75·06 cm. To leave $\overline{w^2}$ largely unaltered while ϵ_w decreases, $\overline{p\,\partial w/\partial z}$ must decrease which also contributes to the rise in $\overline{p\,\partial v/\partial y}$. We reach the intriguing proposition that the redistribution terms, which eventually must transfer energy *away* from the normal component to accommodate the impermeability condition that $V = v = 0$ at the wall, may initially do the opposite in the present flow. In part 2 we show that $\overline{v^2}$ decreases after 100 cm.

Figure 24 shows the balance of the terms in the shear-stress transport equation

$$U\,\frac{\partial(\overline{uv})}{\partial x} + V\,\frac{\partial(\overline{uv})}{\partial y} + \overline{v^2}\,\frac{\partial U}{\partial y} + \frac{\partial}{\partial y}\,(\overline{pu} + \overline{uv^2}) - \overline{p\left(\frac{\partial u}{\partial y} + \frac{\partial v}{\partial x}\right)} = 0; \qquad (11)$$

that is

MEAN TRANSPORT + GENERATION + TURBULENT TRANSPORT + PRESSURE–STRAIN = 0.

Again the calculated $\overline{uv}$ values were used, $\overline{pu}$ was neglected, and the pressure–strain term was found by difference. As the wall becomes important the pressure–strain term increases, while the generation decreases, leaving the level of $\overline{uv}$ unaltered.

Bradshaw & Koh (1981) show that the Poisson equation for the pressure can be written as

$$-\nabla^2(P + p) = E_{ij}E_{ji} - \tfrac{1}{2}\Omega_i^2,$$

where

$$E_{ij} \equiv \tfrac{1}{2}\left[\frac{\partial(U_i + u_i)}{\partial x_j} + \frac{\partial(U_j + u_j)}{\partial x_i}\right]$$

is the instantaneous rate of strain in the (i, j)-plane and Ω_i^2 is the instantaneous total vorticity. The positive contribution from $E^2 \equiv E_{ij}E_{ji}$ arises from eddy 'collisions', that is, saddle points in the instantaneous stream-function pattern. The discussion of (10) and (11) implies that all components of E^2 have been altered as the vertical motion moves to collide with its mirror image. This implication is consistent with the conclusion that the pressure-containing redistribution of normal stress and the pressure–strain terms are significantly altered by the wall.

The behaviour of $\overline{u^2}$ as x increases is quite different from that of $\overline{v^2}$. The increase begins near the high-velocity edge and propagates inward, as suggested by the analyses of Hunt & Graham (1978) and WF, which indicate that the distance to the wall is the important new parameter. As was found by Thomas & Hancock (1978) in their measurements of grid turbulence near a moving wall, $\overline{u^2}$ is amplified considerably more than $\overline{w^2}$, both at constant x and varying η, and at constant η and increasing x, and it does not matter whether the zonal contributions or the total mean-square intensities are considered. This disparity in amplification is in marked contrast to the theories of Hunt & Graham and WF, which predict equal amplification
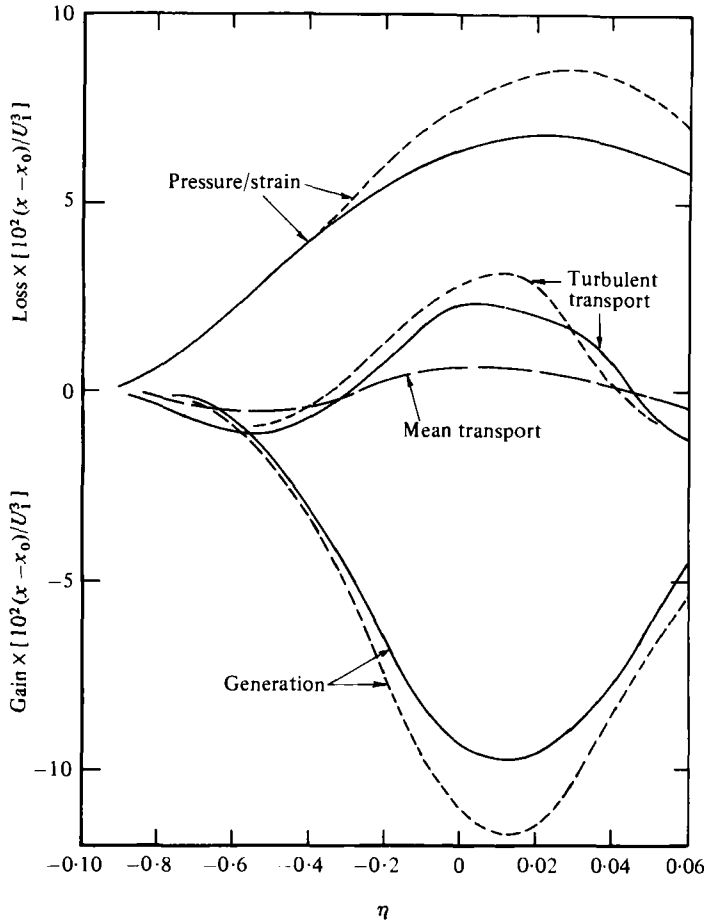
FIGURE 24. Balance of shear stress equation. Solid lines, $x-x_0$ (cm) = 49·51; dashed lines, 75·06. Mean transport is not altered.

of $\overline{u^2}$ and $\overline{w^2}$. In the present flow the reason for the disparity is simply that the large eddies are neither homogeneous in the x-direction (because of shear-layer growth) nor axisymmetric about the z-axis so that the streamwise motion will be preferentially amplified. In the absence of correlation measurements, it is not possible to say whether the results of Thomas & Hancock are also due to this lack of axisymmetry. Since their $\overline{u^2}$, at constant non-dimensional distance from the wall, increased as x increased, it is possible that the usual streamwise decay of grid turbulence, which also was not included in the analysis of Hunt & Graham, was partially responsible for the unequal amplification. The large-eddy simulation of Biringen & Reynolds (1981), which assumed vertical axisymmetry but *not* streamwise homogeneity, reproduced the increase in $\overline{u^2}$, with x, found by Thomas & Hancock.

6. Conclusions

We have shown that significant changes in the structure of a turbulent mixing layer occur as it becomes influenced by a solid surface well before the turbulent region actually reaches the surface. At the same time the mean-velocity profile remains unaltered.

With the exception of the rise in v-spectrum and the unequal amplification of $\overline{u^2}$ and $\overline{w^2}$, the behaviour of the single-point measurements, such as $\overline{u^2}$, the flatness factors and V_q', were explained in terms of the increasing level of fluctuations in the diminishing potential core. The correlation measurements in the unaffected flow showed that the scale of the turbulent contribution to the spanwise correlations did not vary significantly with η, while the potential contribution to these correlations increased enormously as η became large and negative.

There was a significant increase in all the spanwise scales as the flow became affected by the wall. All these results emphasize the essential three-dimensionality of the large-eddy structure in the unaffected flow. This structure appears to be a horseshoe vortex resulting from a combination of Grant's double-roller eddy and an outward motion similar to his mixing jets. The inhomogeneity of the horseshoe vortex in the (x, y)-plane explains the unequal amplification of $\overline{u^2}$ and $\overline{w^2}$.

The wall stretches the double-roller component in the (x, z)-plane and so weakens its y-direction vorticity, allowing the outer motion to become dominant. As the instantaneous mirror-image structure becomes important, the pressure field is altered, and it is suggested that this alteration is primarily responsible for the rise in $\overline{v^2}$ across the whole layer. To avoid significant image effects in single-stream mixing layers it is recommended that measurements be limited to the region where $\delta/h < 0.8$ approximately.

Although the mean-velocity and shear-stress distributions in unperturbed mixing layers, and indeed in the present flow over the range of x studied here, can be easily computed using simple closure assumptions such as a constant eddy viscosity, the present results emphasize the complex response of the turbulence structure to a change in boundary conditions. In particular, it appears that the first effect of the wall is to redistribute the turbulent energy between its components in the opposite direction to that occurring in fully developed wall layers, where the components in the plane of the wall are enhanced at the expense of the normal component.

We note that similar, and perhaps even larger, changes will occur in a two-stream mixing layer confined by a tunnel roof as well as the floor. Such changes may be partially responsible for the large spanwise scales observed by Brown & Roshko (1974) and measured by Wygnanski *et al.* (1979).

Appendix. Intermittency scheme and two-point conditional sampling

The intermittency scheme used is basically the 'signal-or-derivative' method described by Bradshaw & Murlis (1974), used by Castro (1973) and Murlis, Tsai & Bradshaw (1982) and developed further by Muck (1980). The flow is called 'turbulent', and the intermittency function $I(t)$ is set to one if *either* $|\partial uv/\partial t|$ or $|\partial^2 uv/\partial t^2|$ is greater than the threshold values (0·25 or 0·30 respectively of the relevant turbulent zone average). These thresholds were found by Muck (1980) to give reasonable agreement with a temperature-based determination of $I(t)$ over a range of flows. The basic problem in intermittency determination is the conflicting requirements of reducing signal 'dropouts' within what is believed to be genuine turbulence, while retaining details of the interface, whose frequency scale cannot be more than an order of magnitude smaller than the Kolmogorov frequency $\omega_K \equiv (\epsilon/\nu)^{\frac{1}{2}}$. The bulk of the conditionally sampled results were obtained from the two-point measurements, which were digitized at a real-time rate of 8 kHz per channel. For signal-or-derivative methods Muck (1980) recommends the use of a *small* 'hold time', over which $I(t)$ is not allowed to vary, to obtain the best compromise between the two conflicting requirements mentioned above. The hold time Δt used in the present experiment was two digital time increments, and was in the range $0·08 \geqslant U_1 \Delta t/\delta \geqslant 0·013$, with the upper limit occurring at the first measurement station (24 cm) where $\omega_K \Delta t \approx 6$; $\omega_K \Delta t$ increased with increasing x. For fuller details the reader is referred to the papers cited at the beginning of this appendix and to Wood (1980, chap. 3). It is sufficient to note here that the present scheme would have to be glaringly inaccurate to invalidate the main conclusions based on the conditionally-sampled correlation measurements in §4.

The single-point results, digitized at 20 kHz real time per channel, were obtained using the same basic intermittency scheme and therefore using a correspondingly smaller hold time.

The use of turbulent-zone averages in the intermittency scheme needs threshold estimates to start the run, and meant that the scheme could not be used near the extreme edge of the mixing layer. The practical limit was found to be $\eta \approx -0·075$, and even here care had to be taken. The scatter in figure 19 is due largely to the poor choice of starting thresholds, but the rest of the results are not significantly affected by the starting thresholds used.

The single-point program computed zone averages relative to the conventional mean, which allows the addition law

$$\bar{\theta} = \gamma\bar{\theta}_T + (1-\gamma)\,\bar{\theta}_N \tag{A 1}$$

to be applied to any quantity $\theta(t)$. The overbars denote time averages, $\gamma \equiv \overline{I(t)}$ is the intermittency factor and the subscripts T and N denote turbulent and non-turbulent zones respectively. The addition law (A 1) was first used by Dean & Bradshaw (1976), who state some of its advantages over the more complex conditional-sampling relationships used by Kovasznay, Kibens & Blackwelder (1970) and Hedley & Keffer (1974) among others. As shown by the discussion of the flatness factors and turbulent-energy transport velocity in §3, (A 1) allows a simple explanation of the results.

For the two-point measurements, denoting the fixed probe as A and the moving probe as B, the addition law is

$$\overline{\theta_A\theta_B} = \gamma_{AB}(\overline{\theta_A\theta_B})_{TT} + (1-\gamma_A-\gamma_B+\gamma_{AB})\,(\overline{\theta_A\theta_B})_{NN} + (\gamma_A-\gamma_{AB})\,(\overline{\theta_A\theta_B})_{TN}$$
$$+ (\gamma_B-\gamma_{AB})\,(\overline{\theta_A\theta_B})_{NT}, \tag{A 2}$$

where $\gamma_{AB} \equiv \overline{I_A(t)\,I_B(t)}$ and the remainder of the first term on the right-hand side is the product of $\theta_A(t)$ and $\theta_B(t)$ averaged over the times when *both* A and B are turbulent (and $I_A(t) = I_B(t) = 1$). The meaning of the other terms should be clear; note that the first subscript (N or T) always refers to point A. Equation (A 2) reduces to (A 1) if $A = B$ and $\theta_A = \theta_B$, since $\overline{I^2(t)} = \overline{I(t)}$ or $\gamma_{AA} = \gamma$.

In this paper the correlations, denoted R_{ij}, are normalized so that $R_{ij} = 1$ at $r = 0$. Thus

$$R_{ij} \equiv \frac{\overline{u_{i,\,A}\,u_{j,\,B}}}{(\overline{u_{i,\,A}\,u_{j,\,A}}\;\overline{u_{i,\,B}\,u_{j,\,B}})^{\frac{1}{2}}}. \tag{A 3}$$

The major reason for using this definition is that small calibration errors cancel from (A 3). The direction of separation is not specified here. In this paper the correlations are denoted by R_{ij}, with a parenthesis denoting the components of the separation vector.

Now the single-point addition law (A 1) does not apply to terms like $\overline{u^m/v^n}$, where $m, n > 0$, nor does the two-point addition law apply to R_{ij} as defined by (A 3). Equation (A 2) was applied to the numerator of R_{ij} only, which is the covariance. To show how this was done we start with the equation for the product of the total velocities at A and B ($\hat{U}_i \equiv U_i + u_i(t)$ and $\hat{U}_j \equiv U_j + u_j(t)$ respectively) and drop the subscripts A and B. It is

$$\hat{U}_i(t)\,\hat{U}_j(t) = \{I_A(t)\,[U_i + u_i(t)] + [1 - I_A(t)]\,[\dot{U}_i + u_i(t)]\}$$

$$\times \{I_B(t)\,[U_j + u_j(t)] + [1 - I_B(t)]\,[U_j + u_j(t)]\}. \tag{A 4}$$

On time averaging, the term containing γ_{AB} becomes

$$\gamma_{AB}[U_i U_j + U_i(U_{j,\,\mathrm{TT}} - U_j) + U_j(U_{i,\,\mathrm{TT}} - U_i) + \overline{u_i u_{j,\,\mathrm{TT}}}],$$

so the turbulent/turbulent (TT) contribution to $\overline{u_i u_j}$, which is $\gamma_{AB}\,\overline{u_i u_{j,\,\mathrm{TT}}}$ (see (A 2)), was found after U_i, U_j, $U_{i,\,\mathrm{TT}}$ and $U_{j,\,\mathrm{TT}}$ were computed independently using

$$\overline{I_A(t)\,I_B(t)\,U_i u_j} = \gamma_{AB} U_i(U_{j,\,\mathrm{TT}} - U_j)$$

and similar relations. The other terms in (A 2) for $\theta_A = U_i$ and $\theta_B = U_j$ were found from (A 4) in a similar manner. Dividing through by the denominator in (A 3) gives the *contributions* to R_{ij}:

$$R_{ij} = R_{i\mathrm{T}j\mathrm{T}} + R_{i\mathrm{N}j\mathrm{N}} + R_{i\mathrm{T}j\mathrm{N}} + R_{i\mathrm{N}j\mathrm{T}}, \tag{A 5}$$

where

$$R_{i\mathrm{T}j\mathrm{T}} = \gamma_{AB}(\overline{u_i u_j})_{\mathrm{TT}}/(\overline{u_{i,\,A}\,u_{j,\,A}}\;\overline{u_{i,\,B}\,u_{j,\,B}})^{\frac{1}{2}},$$

$$R_{i\mathrm{N}j\mathrm{N}} = (1 - \gamma_A - \gamma_B + \gamma_{AB})\,(\overline{u_i u_j})_{\mathrm{NN}}/(\overline{u_{i,\,A}\,u_{j,\,A}}\;\overline{u_{i,\,B}\,u_{j,\,B}})^{\frac{1}{2}},$$

and similarly for the other terms, as defined by this procedure. As the probe separation decreases, the TT and non-turbulent/non-turbulent (NN) contributions must asymptote to the single-point results for probe A. The results for probe A are plotted in §4 and serve as a check on the accuracy of the two-point conditional-sampling routines, but obviously *not* on the accuracy of intermittency determination. As the probe separation decreases, the turbulent/non-turbulent (TN) and NT contributions asymptote to zero as can be seen by comparing (A 1) and (A 2). The

correlation of the intermittency functions

$$R_{II} \equiv \frac{\overline{[I_A(t)-\gamma_A][I_B(t)-\gamma_B]}}{\{\overline{[I_A(t)-\gamma_A]^2}\,\overline{[I_B(t)-\gamma_B]^2}\}^{\frac{1}{2}}} = \frac{\gamma_{AB}-\gamma_A\gamma_B}{(\gamma_A-\gamma_A^2)^{\frac{1}{2}}(\gamma_B-\gamma_B^2)^{\frac{1}{2}}} \tag{A 6}$$

was also computed. Equation (A 6) has the same form as (A 3) and is 1 if $I_A(t) = I_B(t)$ and zero if $I_A(t)$ and $I_B(t)$ are uncorrelated. The definition of R_{II} is the same as that used by Kovasznay *et al.* (1970).

REFERENCES

BIRCH, S. F. 1980 Planar mixing layer data evaluation for AFOSR-HTTM-Stanford Conf. on Complex Turbulent Flow.

BIRINGEN, S. & REYNOLDS, W. C. 1981 *J. Fluid Mech.* **103**, 53.

BRADSHAW, P. 1966 *J. Fluid Mech.* **26**, 255.

BRADSHAW, P. 1967 *J. Fluid Mech.* **30**, 241.

BRADSHAW, P. 1972 *Imperial College Aero Rep.* no. 72-10.

BRADSHAW, P. 1973 *Imperial College Aero Rep.* no. 73-05. London.

BRADSHAW, P. 1975 *Trans. A.S.M.E.* I: *J. Fluids Engng* **97**, 146.

BRADSHAW, P. 1976 In *Proc. 14th Int. Congr. Appl. Mech.* (Ed. W. T. Koiter), p. 101. North-Holland.

BRADSHAW, P. 1980 Introduction to section on 'Coherent Structures'. In *Turbulent Shear Flows 2* (ed. L. J. S. Bradbury, F. Durst, B. E. Launder, F. W. Schmidt & J. H. Whitelaw), p. 259. Springer.

BRADSHAW, P., FERRISS, D. H. & JOHNSON, R. F. 1964 *J. Fluid Mech.* **19**, 51.

BRADSHAW, P. & KOH, Y. M. 1981 *Phys. Fluids* **24**, 777.

BRADSHAW, P. & MURLIS, J. 1974 *Imperial College Aero Rep.* no. 74-04.

BROWAND, F. K. & LATIGO, B. O. 1979 *Phys. Fluids* **22**, 1011.

BROWN, G. L. & ROSHKO, A. 1974 *J. Fluid Mech.* **64**, 715.

CASTRO, I. 1973 A highly-distorted turbulent free shear layer. Ph.D. thesis, Imperial College, London.

CASTRO, I. & BRADSHAW, P. 1976 *J. Fluid Mech.* **73**, 265.

CHANDRSUDA, C. & BRADSHAW, P. 1981 *J. Fluid Mech.* **110**, 171.

CHANDRSUDA, C., MEHTA, R. D., WEIR, A. D. & BRADSHAW, P. 1978 *J. Fluid Mech.* **85**, 693.

CORRSIN, S. & KISTLER, A. L. 1955 *NACA Rep.* no. 1244.

DEAN, R. B. & BRADSHAW, P. 1976 *J. Fluid Mech.* **76**, 241.

GRANT, H. L. 1958 *J. Fluid Mech.* **4**, 149.

GUTMARK, E., WOLFSTEIN, M. & WYGNANSKI, I. 1978 *J. Fluid Mech.* **88**, 737.

HEDLEY, T. B. & KEFFER, J. F. 1974 *J. Fluid Mech.* **64**, 625.

HUNT, J. C. R. & GRAHAM, J. M. R. 1978 *J. Fluid Mech.* **84**, 209.

KOVASZNAY, L. S. G., KIBENS, V. & BLACKWELDER, R. F. 1970 *J. Fluid Mech.* **41**, 283.

LAUNDER, B. E., REECE, G. J. & RODI, W. 1975 *J. Fluid Mech.* **68**, 537.

MUCK KIN-CHOONG 1980 *Imperial College Aero Rep.* no. 80-03.

MURLIS, J., TSAI, H. M. & BRADSHAW, P. 1982 *J. Fluid Mech.* **122**, 13.

PHILLIPS, O. M. 1955 *Proc. Camb. Phil. Soc.* **51**, 220.

PUI, N. K. & GARTSHORE, I. S. 1979 *J. Fluid Mech.* **91**, 111.

RODI, W. 1973 In *Studies in Convection* (ed. B. E. Launder), vol. 1, p. 79. Academic.

ROSHKO, A. 1976 *A.I.A.A. J.* **14**, 1349.

SMITS, A. J., YOUNG, S. T. B. & BRADSHAW, P. 1979 *J. Fluid Mech.* **82**, 481.

THOMAS, N. H. & HANCOCK, P. E. 1978 *J. Fluid Mech.* **82**, 481.

TOWNSEND, A. A. 1961 *J. Fluid Mech.* **11**, 97.

TOWNSEND, A. A. 1976 *The Structure of Turbulent Shear Flow*, 2nd ed. Cambridge University Press.

UZKAN, T. & REYNOLDS, W. C. 1967 *J. Fluid Mech.* **37**, 95.

VAN ATTA, C. W., SOKOLOV, M., ANTONIA, R. A. & CHAMBERS, A. J. 1982 *Phys. Fluids.* **25**, 424.

WEBER, D. P. 1974 Turbulent velocity field structure in a round jet. Ph.D. thesis, University of Illinois at Urbana Champaign.

WEIR, A. D. & BRADSHAW, P. 1974 *Imperial College Aero Rep.* no. 74–09.

WEIR, A. D., WOOD, D. H. & BRADSHAW, P. 1981 *J. Fluid Mech.* **107**, 237.

WILLS, J. A. B. 1964 *J. Fluid Mech.* **20**, 417.

WOOD, D. H. 1980 A reattaching, turbulent, thin shear layer. Ph.D. thesis, Imperial College, London.

WOOD, D. H. 1982 Spanwise non-uniformities in a nominally plane mixing layer. *T.N.-F.M. University of Newcastle, Australia.*

WOOD, D. H. & FERZIGER, J. H. 1981 The potential flow bounded by a mixing layer and a solid surface. Submitted to *J. Fluid Mech.*

WYGNANSKI, I. & FIEDLER, H. E. 1970 *J. Fluid Mech.* **41**, 229.

WYGNANSKI, I., OSTER, D., FIEDLER, H. E. & DZIOMBA, B. 1979 *J. Fluid Mech.* **93**, 325.

YULE, A. J. 1978 *J. Fluid Mech.* **88**, 413.